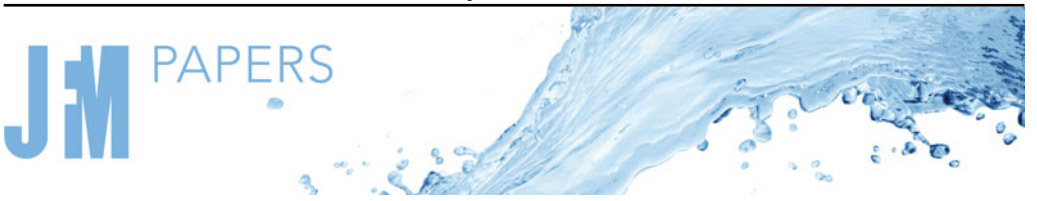
J. Fluid Mech. (2026), *vol.* 1026, A28, doi:10.1017/jfm.2025.11048



The action of spatial modulation of a transverse temperature gradient on floating droplets dynamics

Alexander A. Nepomnyashchy[1] **and Ilya B. Simanovskii**[1]

[1]Department of Mathematics, Technion – Israel Institute of Technology, 32000 Haifa, Israel

Corresponding author: Ilya B. Simanovskii, yuri11@inter.net.il

(Received 5 May 2025; revised 18 November 2025; accepted 10 December 2025)

The instabilities of a floating droplet under the action of an inclined temperature gradient in the presence of the spatial modulation of the transverse temperature gradient are investigated. The problem is studied numerically in the framework of the slender droplet approximation and the precursor model. It is shown that the spatial modulation of the transverse component of the Marangoni number is accompanied by the change of the droplet shape and can lead to development of periodic oscillations. In the definite region of parameters, quasi-periodic oscillations accompanied by the creation of pulsating satellites have been obtained. The separation and the recombination of the 'main' droplet with the satellites have been observed.

Key words: interfacial flows (free surface), nonlinear instability

1. Introduction

The Marangoni convection in liquid layers has been studied extensively in the past few decades, due to its importance in microgravity engineering and microfluidics. Two basic cases have been investigated: (i) the case where a temperature gradient is applied across the layer; (ii) the case where a temperature gradient is applied along the layer (for a review, see Simanovskii & Nepomnyashchy 1993; Nepomnyashchy, Simanovskii & Legros 2012).

There are two basic modes of Marangoni instabilities in a liquid layer heated from below: (i) the 'Pearson mode' (Pearson 1958) and (ii) the 'Scriven–Sternling mode' (Scriven & Sternling 1964). The Pearson instability mechanism is observed in relatively thick layers, while the Scriven–Sternling mechanism takes place under microgravity conditions or in very thin layers (Van Hook *et al.* 1995, 1997). The interplay between the Marangoni instability caused by the transverse component of the temperature gradient and the thermocapillary flow generated by the longitudinal component of the temperature gradient can lead to much more complex dynamics and

© The Author(s), 2026. Published by Cambridge University Press.

https://doi.org/10.1017/jfm.2025.11048 Published online by Cambridge University Press

unexpected effects. When the imposed gradient is inclined with respect to the interface, the Marangoni instability is developed on the background of a parallel thermocapillary flow generated by the horizontal component of the temperature gradient. The problem when an imposed gradient is inclined with respect to the interface in the case of a non-deformable interface has been investigated by Davis (1987) for a single layer, and by Nepomnyashchy, Simanovskii & Braverman (2001) for a two-layer system. The problem has also been studied experimentally by Ueno, Kurosawa & Kawamura (2002). The longwave deformational Marangoni instability in two-layer films under the action of an inclined temperature gradient has been studied by Nepomnyashchy & Simanovskii (2009*a*,*b*). Oscillatory convective flows generated by the thermocapillary effect and buoyancy have been observed in some experiments (Rybalko, Magome & Yoshikawa 2004; Song *et al.* 2014; Buffone 2019). Earlier numerical and experimental works have explored thermocapillary propulsion with non-uniform heating in thin films (see Zheng & Stone (2021) and references therein).

Analysis of floating droplets, when a droplet of one liquid floats on the liquid substrate of another liquid ('liquid lenses') was started in the context of spreading (Suciu, Smigelschi & Ruckenstein 1970; Bacri, Debrégeas & Brochard-Wyart 1996), wetting (Joanny 1987) and dewetting (Brochard Wyart, Martin & Redon 1993). Instabilities similar to those observed in two-layer films have also been obtained in floating droplets (for a review, see Nepomnyashchy 2021). Droplets on a liquid substrate play an important role in various branches of engineering, including microfluidics (Labanieh *et al.* 2015), chemical engineering (Yamini, Rezazadeh & Seidi 2019) and environment protection (Ju *et al.* 2019).

Droplets on a liquid substrate can be considered as a two-layer films. The same equations are used in the whole region, but outside the droplet, where the top layer is ultra-thin, the corresponding disjoining pressure is taken into account.

In applications (e.g. in microfluidic devices), it can be necessary to move a droplet in a controllable way. The simplest way to influence the dynamics of a droplet is a temperature inhomogeneity that creates a Marangoni flow. Typically, the droplet is advected by the thermocapillary motion in the liquid layer in the direction opposite to the surface temperature gradient, but there is a contribution to the droplet velocity due to the thermocapillary stresses on the droplet interfaces and due to the shear in the substrate liquid (Greco & Grigoriev 2009). The direction of motion can be different depending on the details of the generated convective flow (Rybalko *et al.* 2004) and the droplet shape (Yakshi-Tafti, Cho & Kumar 2010).

The influence of homogeneous cooling or heating of the liquid substrate on the stability of a floating droplet has been considered by Nepomnyashchy & Simanovskii (2021). The suppression and the excitation of oscillations under the action of an inclined temperature gradient have been studied by Nepomnyashchy & Simanovskii (2025). The observed instabilities of droplets are reminiscent of longwave deformational instabilities in two-layer films (Nepomnyashchy & Simanovskii 2007).

The present paper is devoted to the investigation of the dynamics and instabilities of the droplets on the liquid substrate under the action of an inclined temperature gradient in the presence of the spatial modulation of the transverse temperature gradient.

It is shown that in a contradistinction to the case of a vertical temperature gradient, the regimes of travelling droplets prevail. In the latter case, some qualitatively new phenomena are expected due to the action of the thermocapillary flow in the liquid substrate on the droplet dynamics, as well as the influence of the flows in the substrate and in the droplet on the development of the Marangoni instability.

https://doi.org/10.1017/jfm.2025.11048 Published online by Cambridge University Press

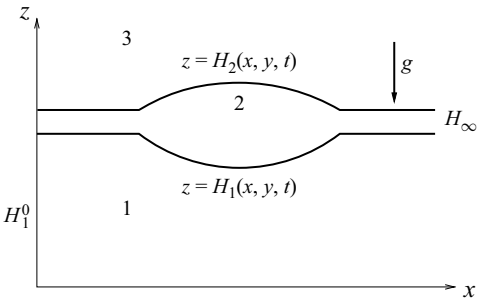


Figure 1. Geometric configuration of the region and coordinate axes.

The structure of the paper is as follows. The mathematical model is presented in § 2. The nonlinear regimes are described in § 3. Specifically, the action of the spatial inhomogeneity of the transverse temperature gradient on the droplets dynamics is described in this section. The action of the gravity force on the droplet shape is discussed in § 4. The influence of the period of spatial modulation and the initial droplet radius on the droplet shape is considered in § 5. Some concluding remarks are given in § 6. The paper also contains an Appendix with more details on the numerical scheme and the validation of the results.

2. Formulation of the problem

We consider a droplet of liquid 2 that floats on a layer of liquid 1. The droplet is in contact with the gas phase 3 (see figure 1). We do not consider any processes in fluid 3: the viscous stresses are neglected at the liquid/gas interface, and the heat transfer is described using the heat exchange coefficient q. The mth fluid has density ρ_m, dynamic viscosity η_m, and thermal conductivity κ_m, $m = 1, 2$.

The temperature of the solid substrate is $T_s + \tilde{A}x$, and the temperature of the gas near the interface is $T_g + \tilde{A}x$. It is assumed that the interfacial tension coefficients on the lower and upper surfaces of the droplet are the linear functions of temperature T: $\sigma_1 = \sigma_1^0 - \alpha_1 T$, $\sigma_2 = \sigma_2^0 - \alpha_2 T$, where α_1 and α_2 are constants. For the description of a floating droplet, we use the precursor model: the interface between fluids 1 and 3 outside the droplet is replaced by an ultra-thin precursor layer of fluid 2 (see figure 1). Far from the droplet, the equilibrium thickness of layer 1 is H_1^0, and the thickness of the precursor film is H_∞. The deformable interfaces are described by equations $z = H_1(x, y, t)$ and $z = H_2(x, y, t)$. The gravity acceleration is g. We assume that the characteristic horizontal scale of the interface deformations is large compared to the characteristic vertical size of the droplet and the liquid substrate. In this case, the nonlinear models governing three-dimensional flows with deformable interfaces can be drastically simplified by the use of the lubrication approximation (see Pototsky *et al.* 2005; Nepomnyashchy & Simanovskii 2007). In the framework of the longwave approach, the shapes of the interfaces $z = H_1$ and $z = H_2$ depend on the scaled horizontal coordinates $X = \epsilon x$ and $Y = \epsilon y$, $\epsilon \ll 1$, rather than on x and y. Also, it is assumed that they depend on the scaled time variable $\tau = \epsilon^2 t$. There are several conditions for the applicability of that approach. First, the surface tension has to be strong, so that any shortwave deformation of the interfaces is suppressed. The analysis (see Oron, Davis & Bankoff 1997) shows that the ratio of the characteristic thickness of the system in the vertical direction to the characteristic scale of the interfacial deformations in the horizontal direction is $O(\epsilon)$, $\epsilon \ll 1$, if the surface tension is $O(\epsilon^{-1/2})$. Also, the droplet

https://doi.org/10.1017/jfm.2025.11048 Published online by Cambridge University Press

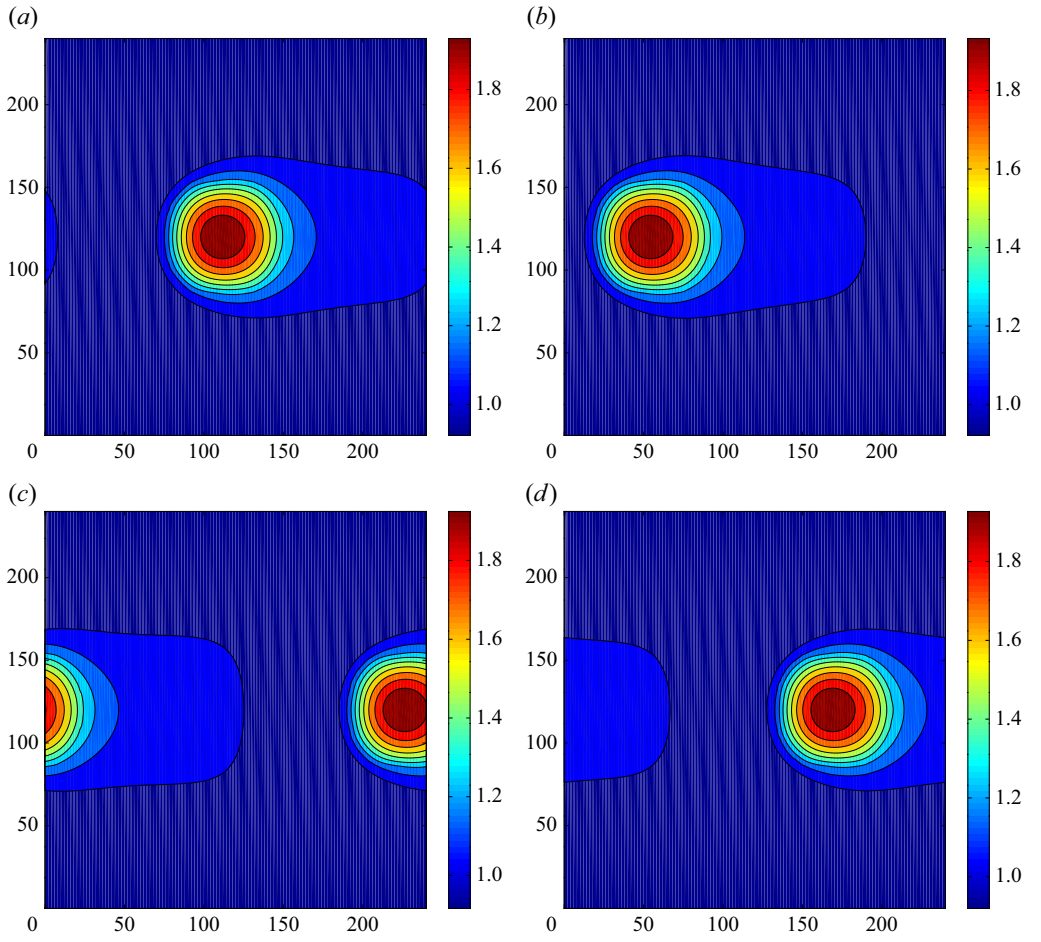


Figure 2. The fields of $h_2(X, Y, \tau)$ for $M_\perp = -0.1$, $M_\parallel = 0.0001$, $Bo = 0$, $Bi = 20$, for (*a*) $\tau = 780\,000$, (*b*) $\tau = 860\,000$, (*c*) $\tau = 930\,000$, (*d*) $\tau = 1 \times 10^6$.

has to be slender due to a small negative spreading coefficient or because of the action of the gravity. In that case, the velocity, pressure and temperature fields are enslaved to the interfacial deformations (see Pototsky *et al.* 2005). That circumstance allows us to reduce the difficult nonlinear problem to a closed system of evolution equations for variables that describe the shapes of interfaces.

The non-dimensional system of equations looks as follows (lowercase letters correspond to non-dimensional quantities):

$$h_{1\tau} + \nabla \cdot \boldsymbol{q}_1 = 0, \quad h_{2\tau} + \nabla \cdot \boldsymbol{q}_2 = 0, \tag{2.1}$$

$$\boldsymbol{q}_1 = f_{11}\nabla\bar{p}_1 + f_{12}\nabla\bar{p}_2 + \boldsymbol{q}_1^T, \quad \boldsymbol{q}_2 = f_{21}\nabla\bar{p}_1 + f_{22}\nabla\bar{p}_2 + \boldsymbol{q}_2^T, \tag{2.2}$$

$$f_{11} = -\frac{1}{3}h_1^3, \quad f_{12} = -\frac{1}{2}h_1^2(h_2 - h_1), \tag{2.3}$$

$$f_{21} = \frac{1}{6}h_1^3 - \frac{1}{2}h_1^2 h_2, \quad f_{22} = (h_2 - h_1)\left[h_1^2\left(\frac{1}{2} - \frac{\eta}{3}\right) + h_1 h_2\left(-1 + \frac{2\eta}{3}\right) - \frac{\eta}{3}h_2^2\right], \tag{2.4}$$

https://doi.org/10.1017/jfm.2025.11048 Published online by Cambridge University Press

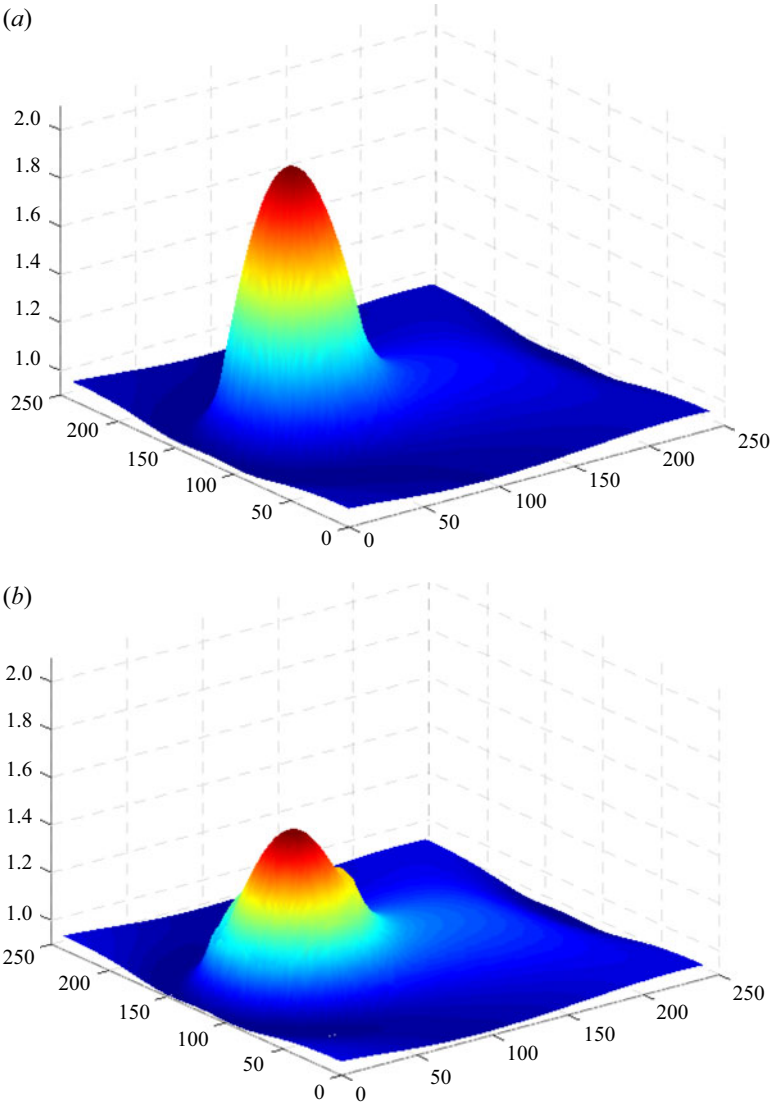


Figure 3. The shapes of interfaces (*a*) $h_2(X, Y, \tau)$ and (*b*) $h_1(X, Y, \tau)$ for $M_\perp = -0.1$, $M_\parallel = 0.0001$, $Bo = 0$, $Bi = 20$, $\tau = 860\,000$.

$$\bar{p}_1 = -\nabla^2 h_1 - \sigma \nabla^2 h_2 + Boh_1 + Bo\rho(h_2 - h_1) + \pi_1(h_1, h_2), \tag{2.5}$$

$$\bar{p}_2 = -\sigma \nabla^2 h_2 + Bo\rho h_2 + \pi_2(h_1, h_2), \tag{2.6}$$

$$\boldsymbol{q}_1^T = \frac{M_\perp}{2} h_1^2 \, \boldsymbol{\nabla}[d(Bih_1 - \alpha\kappa)] - \frac{M_\parallel}{2}(1+\alpha) h_1^2 \boldsymbol{e}_x, \tag{2.7}$$

$$\begin{aligned} \boldsymbol{q}_2^T = {} & \frac{M_\perp}{2}\big\{ - h_2^2 \, \boldsymbol{\nabla}(d\eta\alpha\kappa) + (2h_2 - h_1) h_1 \, \boldsymbol{\nabla}\{d[Bih_1 - \alpha\kappa(1-\eta)]\}\big\}, \\ & - \frac{M_\parallel}{2}\big[\eta\alpha(h_2 - h_1)^2 + (1+\alpha) h_1 (2h_2 - h_1)\big]\boldsymbol{e}_x, \end{aligned} \tag{2.8}$$

$$d = [\kappa + Bi(1-\kappa)h_1 + Bi\kappa h_2]^{-1}. \tag{2.9}$$

https://doi.org/10.1017/jfm.2025.11048 Published online by Cambridge University Press

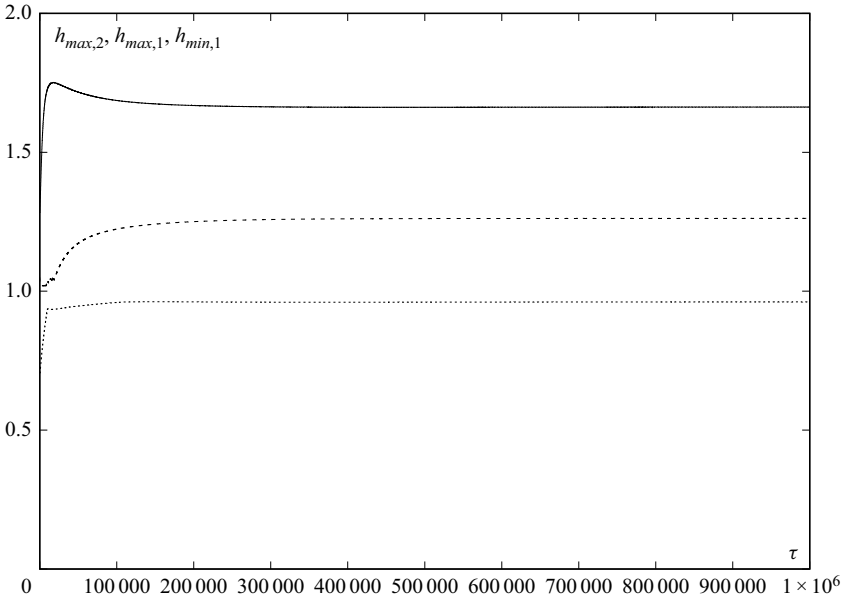


Figure 4. The dependences of $h_{max,2}(\tau)$ (solid line), $h_{max,1}(\tau)$ (dashed line) and $h_{min,1}(\tau)$ (dotted line) on time for $M_\perp = -0.1$, $M_\parallel = 0.0001$, $Bo = 0.02$, $Bi = 20$.

Let us note that the system of equations describing the dynamics in the longwave limit is invariant with respect to the scaling transformation

$$X \to cX, \quad \tau \to c^4\tau, \quad p_j \to c^2 p_j, \quad \boldsymbol{q}_j \to c^3 \boldsymbol{q}_j, \quad M_\perp \to c^2 M_\perp, \quad M_\parallel \to c^3 M_\parallel, \tag{2.10}$$

$$Bo \to c^2 Bo, \tag{2.11}$$

where c is an arbitrary number (see Nepomnyashchy & Simanovskii 2012). This means that in the case of a layer that is infinite in the horizontal direction, all the results obtained for definite values of the parameters ($M_\perp$, $M_\parallel$, Bo) can be applied for the other sets of parameters found according to (2.10). That scaling invariance is caused by the absence of a characteristic horizontal length scale in the case of an infinite layer. Therefore, the scales for variables τ and p, as well as parameters $M_\perp$, $M_\parallel$ and Bo, contain an arbitrary parameter L^* corresponding to the horizontal length scale.

We choose

$$\tau^* = \frac{\eta_1 (L^*)^4}{\sigma_1^0 \left(H_1^0\right)^3} \tag{2.12}$$

as a time scale, and

$$p^* = \frac{\sigma_1^0 H_1^0}{(L^*)^2} \tag{2.13}$$

as a pressure scale.

The non-dimensional parameters of the problem are

$$M_\perp = \frac{\alpha_1 (T_s - T_g)}{\sigma_1^0} \left(\frac{L^*}{H_1^0}\right)^2, \tag{2.14}$$

https://doi.org/10.1017/jfm.2025.11048 Published online by Cambridge University Press

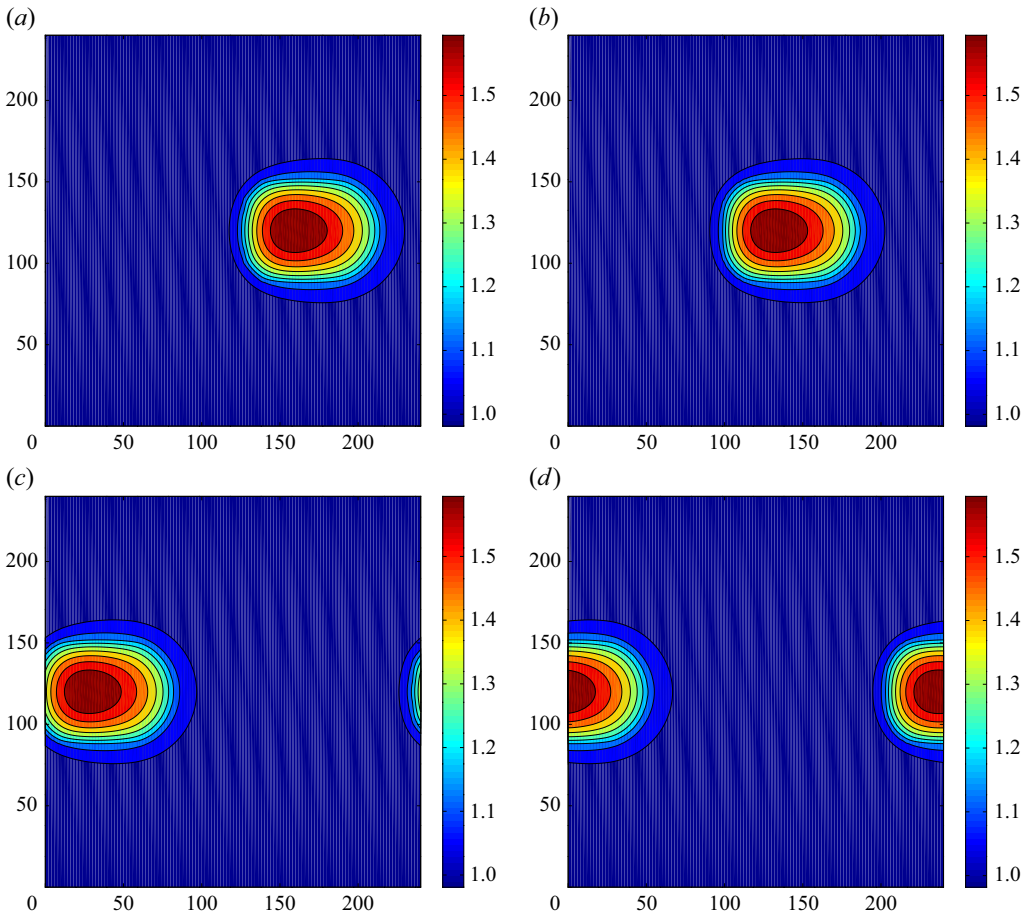


Figure 5. The fields of $h_2(X, Y, \tau)$ for $M_\perp = -0.1$, $M_\parallel = 0.0001$, $Bo = 0.02$, $Bi = 20$, for (*a*) $\tau = 630\,000$, (*b*) $\tau = 710\,000$, (*c*) $\tau = 790\,000$, (*d*) $\tau = 870\,000$.

$$M_\parallel = \frac{\alpha_1 A L^*}{\sigma_1^0}\left(\frac{L^*}{H_1^0}\right)^2 \tag{2.15}$$

as the modified transverse and longitudinal Marangoni numbers, respectively. Also,

$$Bi = \frac{q H_1^0}{\kappa_2} \tag{2.16}$$

is the Biot number, $\eta = \eta_1/\eta_2$, $\kappa = \kappa_1/\kappa_2$, $\sigma = \sigma_2^0/\sigma_1^0$, $\alpha = \alpha_2/\alpha_1$, $\rho = \rho_2/\rho_1$, and

$$Bo = \frac{g\rho_1 (L^*)^2}{\sigma_1^0} \tag{2.17}$$

is the Bond number.

One can see that each flow rate $\boldsymbol{q}_1^T$ and $\boldsymbol{q}_2^T$ contains two contributions, one proportional to $M_\parallel$, and the other to $M_\perp$. The former contribution, which is caused by the imposed horizontal temperature gradient, is always directed opposite to vector $\boldsymbol{e}_x$, i.e. towards the region with lower temperature and hence higher interfacial tensions. Note that the

https://doi.org/10.1017/jfm.2025.11048 Published online by Cambridge University Press

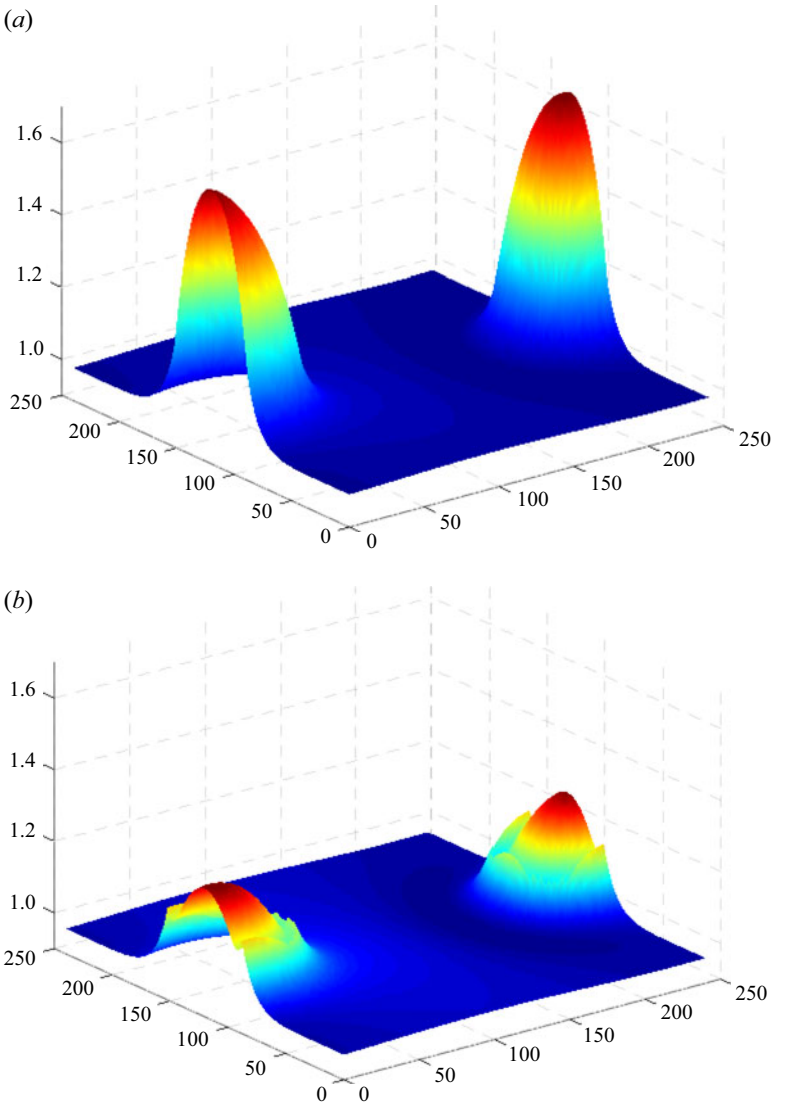


Figure 6. The shapes of interfaces (*a*) $h_2(X, Y, \tau)$ and (*b*) $h_1(X, Y, \tau)$ for $M_\perp = -0.1$, $M_\parallel = 0.0001$, $Bo = 0.02$, $Bi = 20$, $\tau = 870\,000$.

contribution of the horizontal temperature gradient into $\nabla \cdot \boldsymbol{q}_1$ can be written as $u_1 h_{1x}$, where

$$u_1 = -M_\parallel (1 + \alpha) h_1. \tag{2.18}$$

Thus each point of the droplet's bottom surface moves to the left with the velocity (2.18). The term with $M_\parallel$ in the expression for $\nabla \cdot \boldsymbol{q}_2$ is $u_2 h_{2x} + w_2$, where

$$u_2 = -M_\parallel [\eta\alpha(h_2 - h_1) + (1 + \alpha) h_1], \tag{2.19}$$

$$w_2 = M_\parallel [\eta\alpha - (1 + \alpha)](h_2 - h_1) h_{1x}. \tag{2.20}$$

Thus in addition to the motion to the left with velocity (2.19), a point on the top surface of the droplet moves upwards or downwards with velocity (2.20).

https://doi.org/10.1017/jfm.2025.11048 Published online by Cambridge University Press

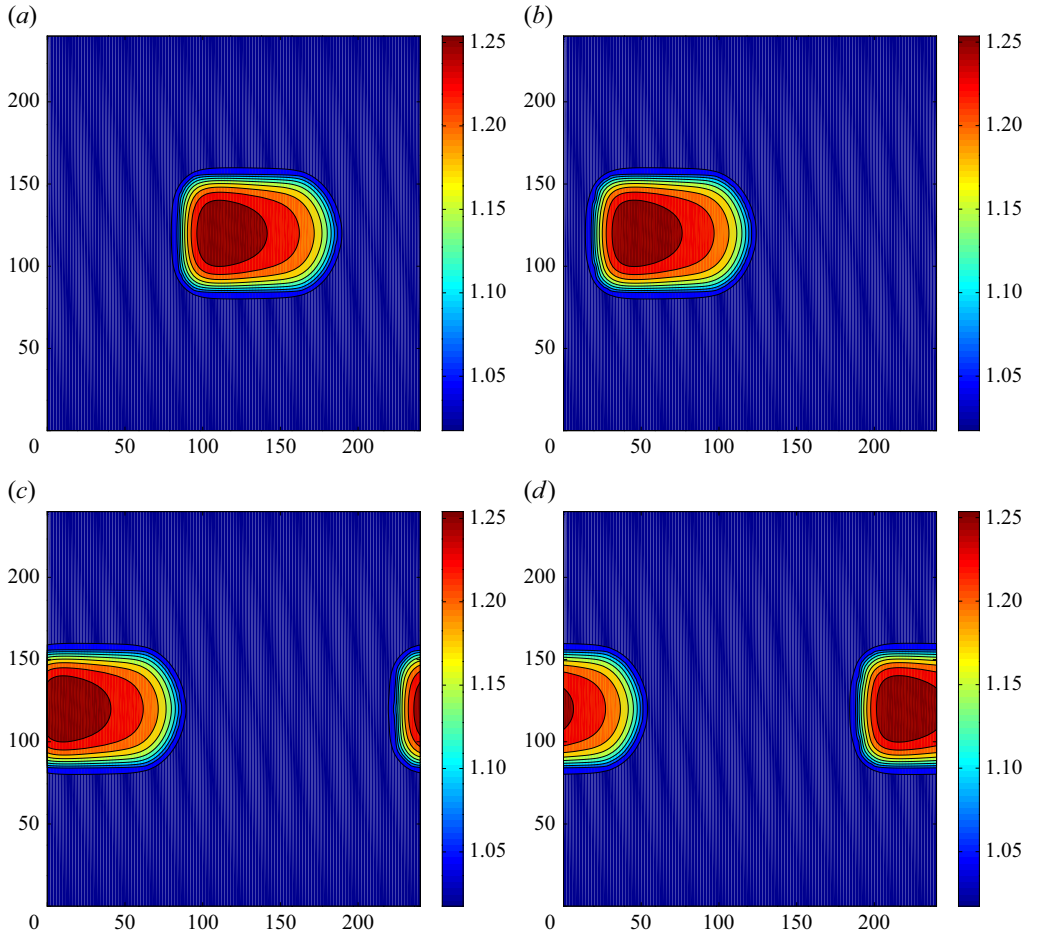


Figure 7. Snapshots of the fields $h_2(X, Y, \tau)$ for $M_\perp = -0.1$, $M_\parallel = 0.0001$, $Bo = 0.1$, $Bi = 20$, for (*a*) $\tau = 700\,000$, (*b*) $\tau = 780\,000$, (*c*) $\tau = 860\,000$, (*d*) $\tau = 940\,000$.

The second contribution, proportional to $M_\perp$, is generated by non-uniformities of the interfacial temperature field, which are caused by the deformations of interfaces.

Because the thickness of liquid layer 1 is always macroscopic, we can neglect the contribution of π_1. In layer 2, we apply the following expression for the disjoining pressure:

$$\pi_2 = \frac{a}{(h_2 - h_1)^3}\left[1 - \left(\frac{h_\infty}{h_2 - h_1}\right)^3\right], \tag{2.21}$$

where a is the non-dimensional Hamaker constant, which is related to the dimensional Hamaker constant A as

$$a = \frac{A(L^*)^2}{6\pi\sigma_1^0\left(H_1^0\right)^4}, \tag{2.22}$$

and $h_\infty = H_\infty / H_1^0$.

https://doi.org/10.1017/jfm.2025.11048 Published online by Cambridge University Press

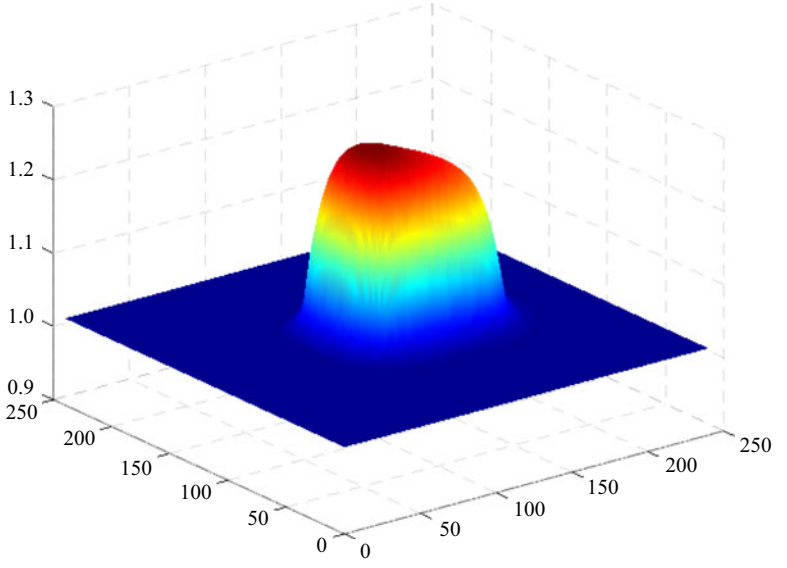


Figure 8. The shape of the interface $h_2(X, Y, \tau)$ for $M_\perp = -0.1$, $M_\parallel = 0.0001$, $Bo = 0.1$, $Bi = 20$, $\tau = 700\,000$.

3. Nonlinear simulations

The problem governed by (2.1)–(2.21) was solved numerically with some initial conditions. The evolution equations were discretised by central differences for spatial derivatives, and solved using an explicit scheme. We use a grid with a constant spatial step, the central differences for spatial derivatives, and the approximation of the first order for temporal derivatives. The explicit scheme is stable for the chosen values of the time step. Periodic boundary conditions have been applied on the boundaries of the computational region $L \times L$. Computations have been performed in the region $L \times L = 240 \times 240$ using the grid 120×120. For moderate values of $M_\perp$ and $M_\parallel$, the fields h_1 and h_2 are rather smooth, thus the grid 120×120 gives a good resolution of large-scale wave patterns. Some trial simulations on the grids 100×100 and 160×160 did not reveal any qualitative changes. More details on the numerical scheme and the validation of the results are presented in the Appendix.

As initial conditions, we use a droplet of liquid 2 with a Gaussian shape that was imposed on a flat layer of liquid 1:

$$h_1(X, Y, 0) = 1, \quad h_2(X, Y, 0) = h_- + h_+ \exp\left\{ -\left[(X - L/2)^2 + (Y - L/2)^2\right]/R^2 \right\}, \tag{3.1}$$

where h_-, h_+ corresponding to the initial shape of the droplet are constants, and R is the radius of the droplet. In some other simulations, in order not to lose the information obtained on the previous time steps, we used as the initial condition a solution formerly obtained for another set of parameters. The computations have been performed for the system of fluorinert FC70 (liquid 1) and silicon oil 10 (liquid 2), which was used in microgravity experiments (see e.g. Géoris *et al.* 1999). The following set of liquid parameters has been applied: $\eta = 3.04$, $\kappa = 0.522$, $\alpha = 2$, $\rho = 0.482$, $\sigma = 2.6$, $h_- = 1.02$, $h_+ = 1$, $R = 20$, $h_\infty = 0.02$ and $Bi = 20$ (see Nepomnyashchy & Simanovskii 2007). The value of a was chosen to be 0.1×10^{-5}. The primary analysis of the obtained nonlinear regimes has been performed using snapshots of the fields of $h_j(X, Y, \tau)$, $j = 1, 2$.

https://doi.org/10.1017/jfm.2025.11048 Published online by Cambridge University Press

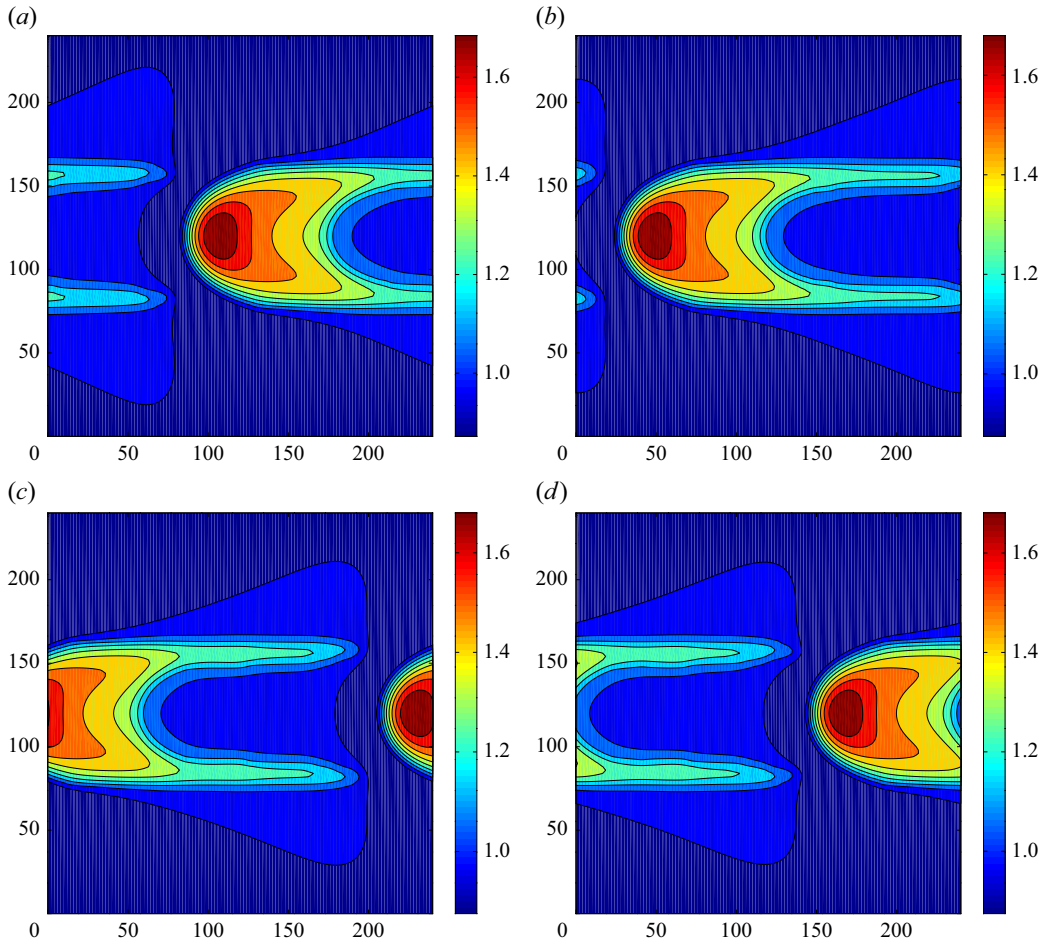


Figure 9. Snapshots of the fields $h_2(X, Y, \tau)$ for $M_\perp = -1$, $M_\parallel = 0.001$, $Bo = 0.02$, $Bi = 20$, for (*a*) $\tau = 2.35 \times 10^6$, (*b*) $\tau = 2.42 \times 10^6$, (*c*) $\tau = 2.49 \times 10^6$, (*d*) $\tau = 2.57 \times 10^6$.

The analysis has been supplemented by the investigation of the time dependence for the maximum values of the variables h_j,

$$h_{max,j}(\tau) = \max h_j(X, Y, \tau), \tag{3.2}$$

and Fourier components

$$c_{m,n}(\tau) = \frac{2}{L^2}\int_0^L\int_0^L h_1(X, Y, \tau)\cos\left[\frac{2\pi X}{L}(mX + nY)\right]\mathrm{d}X\,\mathrm{d}Y, \tag{3.3}$$

$$s_{m,n}(\tau) = \frac{2}{L^2}\int_0^L\int_0^L h_1(X, Y, \tau)\sin\left[\frac{2\pi X}{L}(mX + nY)\right]\mathrm{d}X\,\mathrm{d}Y, \tag{3.4}$$

where m, n are integer numbers.

We have used also quantities

$$r_{m,n}(\tau) = \sqrt{c^2_{m,n}(\tau) + s^2_{m,n}(\tau)}, \tag{3.5}$$

characterising the amplitudes of corresponding complex Fourier harmonics.

https://doi.org/10.1017/jfm.2025.11048 Published online by Cambridge University Press

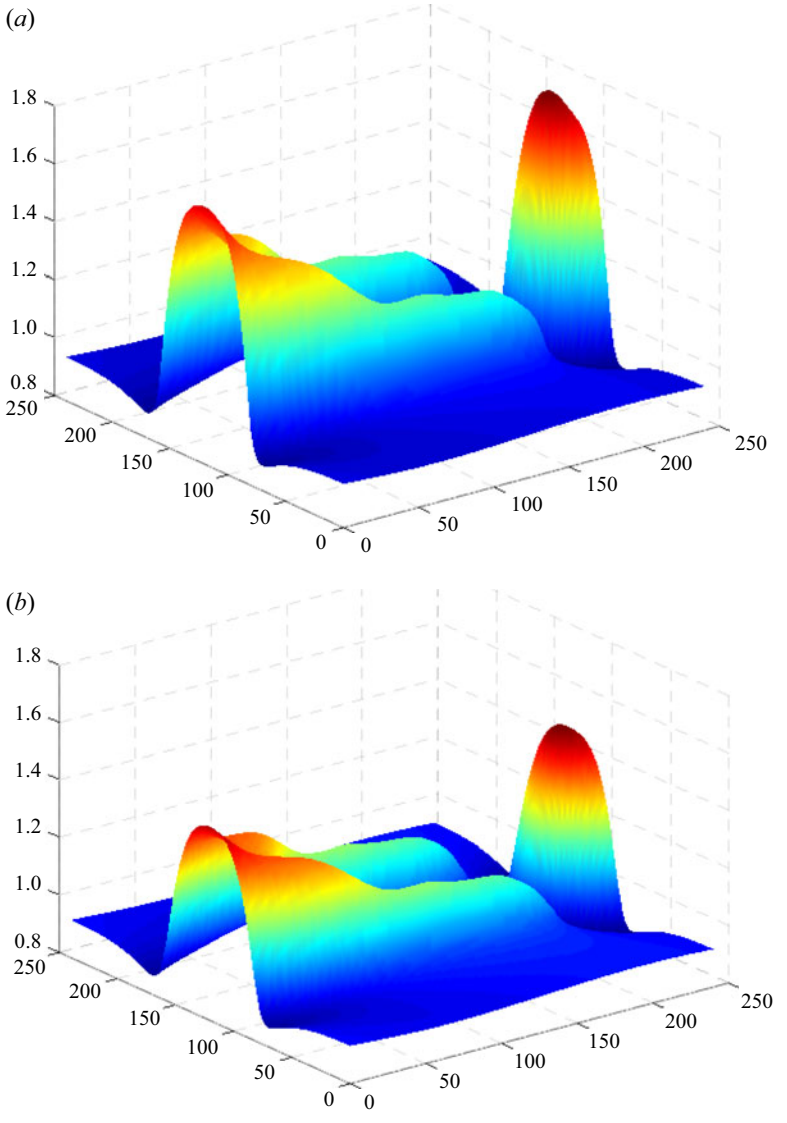


Figure 10. The shapes of interfaces (*a*) $h_2(X, Y, \tau)$ and (*b*) $h_1(X, Y, \tau)$ for $M_\perp = -1$, $M_\parallel = 0.001$, $Bo = 0.02$, $Bi = 20$, $\tau = 2.49 \times 10^6$.

3.1. *The case of a constant temperature gradient*

First, let us describe the results of nonlinear simulations in the case of homogeneous heating. We take $Bo = 0$. The simplest structure observed for sufficiently small values of $M_\parallel$ and $|M_\perp|$ is the droplet, moving from right to left as a whole (Nepomnyashchy & Simanovskii 2025):

$$h_j = h_j(X + c\tau), \quad j = 1, 2, \ c > 0. \tag{3.6}$$

The snapshots of the fields of $h_2(X, Y, \tau)$ at different instants of time are shown in figure 2. In all figures showing the droplet, the horizontal axis is X and the vertical axis is Y. The shapes of interfaces corresponding to figure 2(*b*) are shown in figure 3.

https://doi.org/10.1017/jfm.2025.11048 Published online by Cambridge University Press

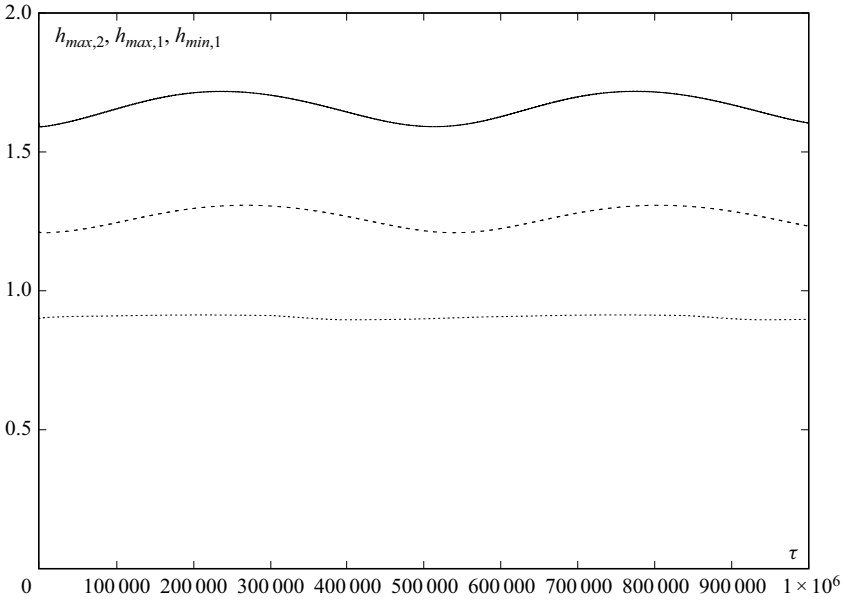


Figure 11. The temporal evolution of $h_{max,2}(\tau)$ (solid line), $h_{max,1}(\tau)$ (dashed line) and $h_{min,1}(\tau)$ (dotted line) for $\bar{M}_\perp = -0.1$, $M_\parallel = 0.0001$, $\Delta_X = 0.025$, $Bo = 0.02$, $Bi = 20$.

This type of motion has also been found in the presence of the gravity force (at $Bo \neq 0$). The temporal evolution of $h_{max,j}$, $j = 1, 2$, and $h_{min,1}$ leading to the formation of the steady droplet is shown in figure 4. The snapshots of $h_2(X, Y, \tau)$ for $Bo = 0.02$ ($M_\perp = -0.1$, $M_\parallel = 0.0001$) are shown in figure 5. As in the previous case, the droplet moves from the right-hand side to the left-hand side. The height of the droplet is lower than that in the case at $Bo = 0$ (cf. for instance, figures 5(b) and 2(a)). The shapes of interfaces corresponding to figure 5(d) are presented in figure 6. At the larger values of the gravity force (we take $Bo = 0.1$), the interfaces of the droplet are essentially flattened. The droplet moves from right to left. The snapshots of $h_2(X, Y, \tau)$ for $Bo = 0.1$ ($M_\perp = -0.1$, $M_\parallel = 0.0001$) are shown in figure 7, and the shape of the interface corresponding to figure 7(a) is shown in figure 8.

Now let us take as the initial conditions the regime presented in figure 6, and consider its evolution at sufficiently large values of $|M_\perp|$ and $M_\parallel$. The snapshots of the fields of $h_2(X, Y, \tau)$ for $M_\perp = -1$ and $M_\parallel = 0.001$ at different instants of time are shown in figure 9. Though the droplet is of a rather complicated ('swallow-like') shape, it moves from the right–hand side to the left–hand side as a whole:

$$h_j = h_j(X + c\tau), \quad j = 1, 2, \ c > 0. \tag{3.7}$$

The shapes of the interfaces corresponding to figure 9(c) are presented in figure 10.

3.2. *The case of a modulated temperature gradient*

Below, we discuss the nonlinear regimes observed in the case of a spatial modulation of the local Marangoni number,

$$M_\perp(X) = \bar{M}_\perp \left(1 + \delta_X \sin \frac{2\pi X}{L}\right) = \bar{M}_\perp - \Delta_X \sin \frac{2\pi X}{L}, \tag{3.8}$$

where $\bar{M}_\perp < 0$, $\delta_X > 0$, $\Delta_X = |\bar{M}_\perp|\, \delta_X$.

https://doi.org/10.1017/jfm.2025.11048 Published online by Cambridge University Press

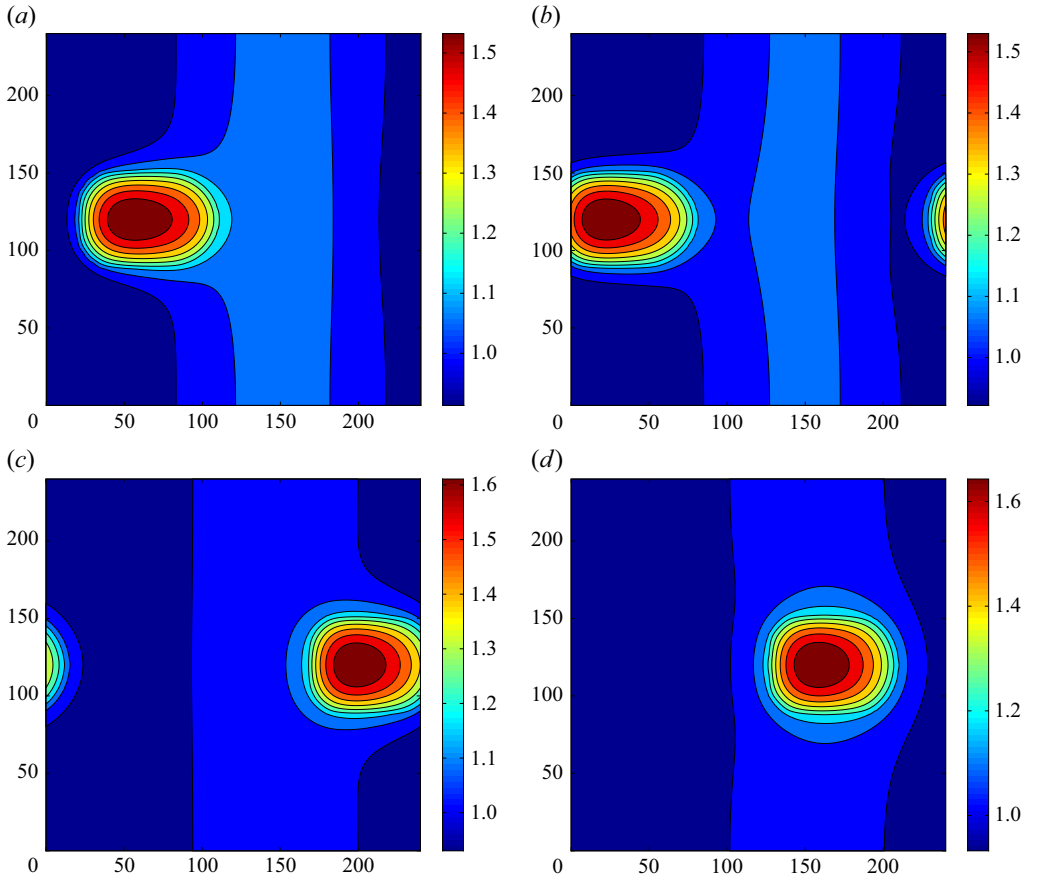


Figure 12. The fields of $h_2(X, Y, \tau)$ for $\bar{M}_\perp = -0.1$, $M_\parallel = 0.0001$, $\Delta_X = 0.025$, $Bo = 0.02$, $Bi = 20$, for (a) $\tau = 330\,000$, (b) $\tau = 468\,500$, (c) $\tau = 607\,000$, (d) $\tau = 744\,500$.

Let us take the droplet presented in figure 5 ($M_\perp = -0.1$, $M_\parallel = 0.0001$, $\Delta_X = 0$) as the initial condition, and consider its evolution under the action of modulation of the transverse Marangoni number ($\bar{M}_\perp = -0.1$, $\Delta_X = 0.025$). The temporal evolution of $h_{max,2}$, $h_{max,1}$ and $h_{min,1}$ is shown in figure 11. One can see that $h_{max,j}$, $j = 1, 2$, and $h_{min,1}$ change in time (cf. figures 4 and 11). The two-dimensional snapshots of the fields $h_2(X, Y, \tau)$ at different instants of time are shown in figure 12. The droplet moves slowly from right to left passing the spatial modulation period L during the time interval $T = 556\,000$. Correspondingly, the shape of the droplet oscillates with the period T. The shapes of the interfaces corresponding to figure 12(a) are presented in figure 13.

With an increase of the transverse Marangoni number (we take $\bar{M}_\perp = -1$), the droplet moving from right to left is significantly deformed. The two-dimensional snapshots of the fields $h_2(X, Y, \tau)$ at different instants of time are shown in figure 14. The shapes of the interfaces corresponding to figure 14(a) are presented in figure 15. One can see that the droplet becomes higher than that in the case $\bar{M}_\perp = -0.1$ (cf. figures 13 and 15).

Let us take as the initial conditions the droplet presented in figures 9(c) and 10, and consider its evolution under the action of the modulation of the transverse temperature gradient ($\Delta_X = 0.025$). The temporal evolution of $h_{max,2}$, $h_{max,1}$ and $h_{min,1}$ is shown in figure 16. One can see that the fields $h_{max,j}$, $j = 1, 2$, and $h_{min,1}$ change in time in a

https://doi.org/10.1017/jfm.2025.11048 Published online by Cambridge University Press

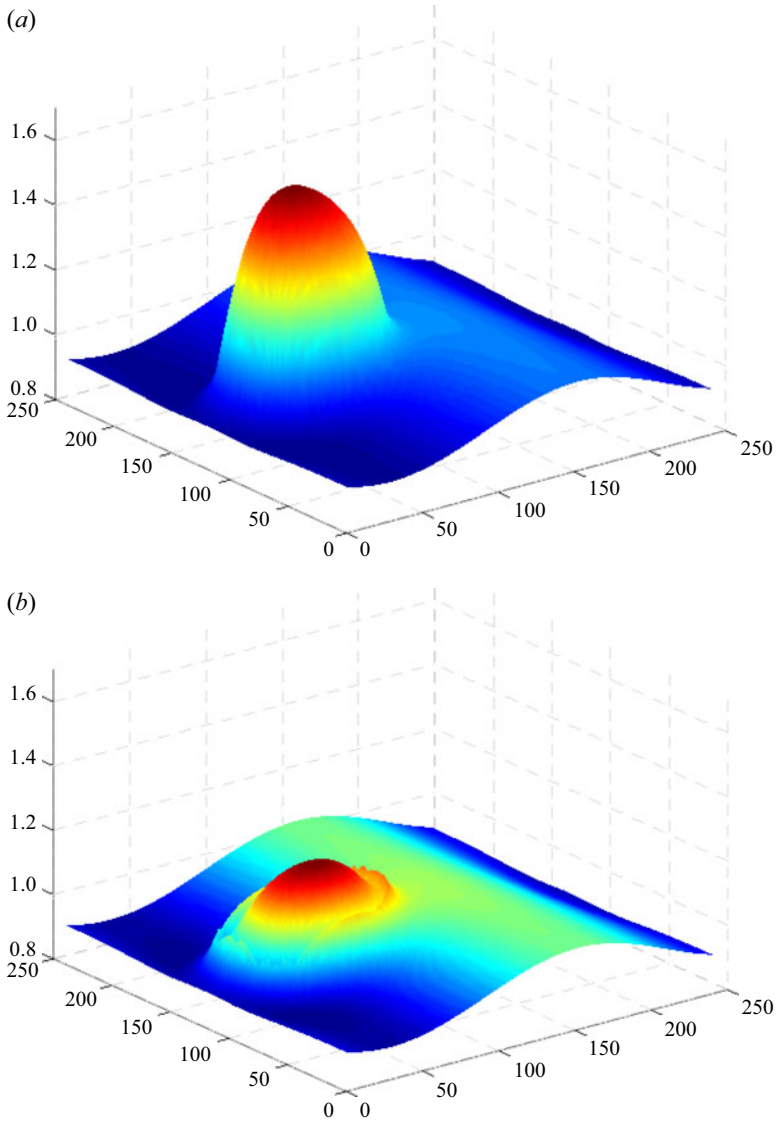


Figure 13. The shapes of interfaces (*a*) $h_2(X, Y, \tau)$ and (*b*) $h_1(X, Y, \tau)$ for $\bar{M}_\perp = -0.1$, $M_\parallel = 0.0001$, $\Delta_X = 0.025$, $Bo = 0.02$, $Bi = 20$, $\tau = 330\,000$.

periodic way. The phase trajectory in the plane (r_{10}, r_{01}) confirms the periodic character of oscillations (see figure 17). The two-dimensional snapshots of the fields $h_2(X, Y, \tau)$ at different instants of time are shown in figure 18, and three-dimensional shapes of interfaces corresponding to figure 18(*e*) are presented in figure 19. The droplet moves from right to left changing the shape during the oscillatory process. During the period of oscillations $T = 41\,850$, the droplet passes the distance L equal to the spatial period of the temperature modulation.

Let us now increase the transverse temperature modulation – we take $\Delta_X = 0.05$ ($\bar{M}_\perp = -1$, $M_\parallel = 0.001$). Since one of the frequencies is due to the instability and the other is due to the passing the temperature modulation period L by the droplet, we observe quasi-periodic oscillations. The temporal evolution of $h_{max,2}$, $h_{max,1}$ and $h_{min,1}$ is shown in

https://doi.org/10.1017/jfm.2025.11048 Published online by Cambridge University Press

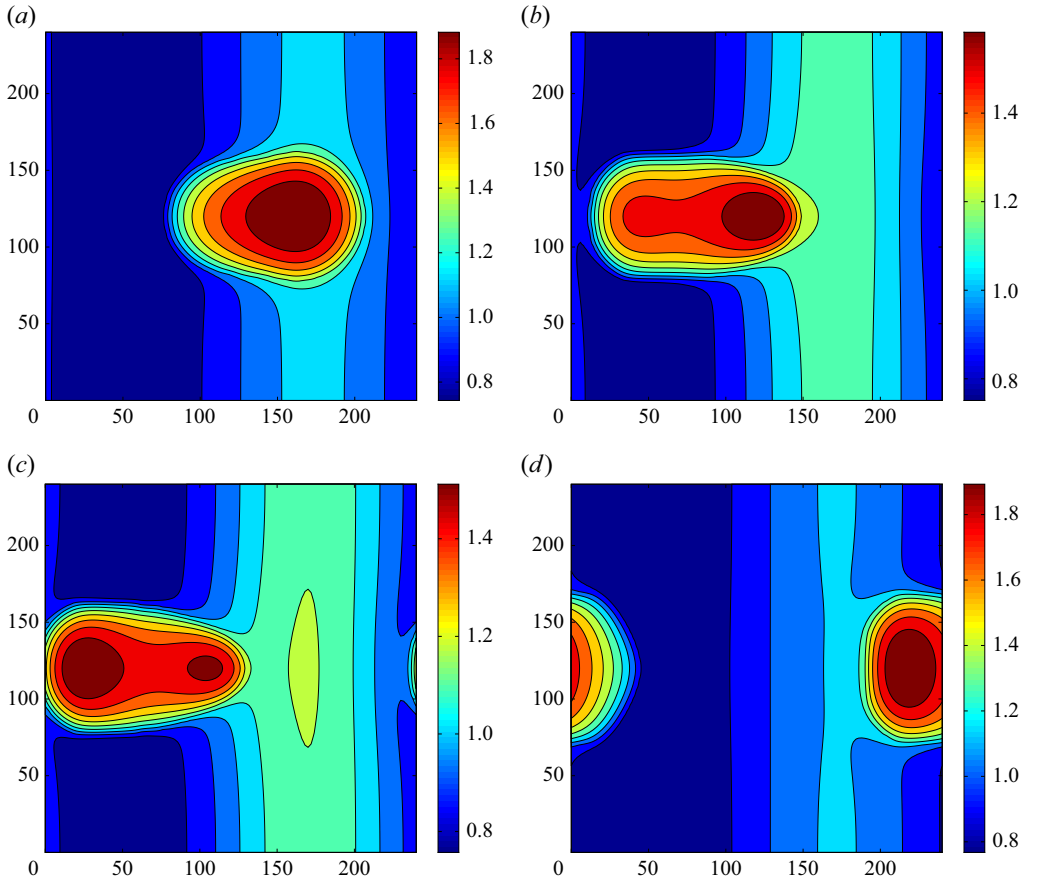


Figure 14. The fields of $h_2(X, Y, \tau)$ for $\bar{M}_\perp = -1$, $M_\parallel = 0.0001$, $\Delta_X = 0.025$, $Bo = 0.02$, $Bi = 20$, for (*a*) $\tau = 150\,000$, (*b*) $\tau = 200\,000$, (*c*) $\tau = 235\,000$, (*d*) $\tau = 285\,000$.

figure 20. Different maxima of $h_{max,j}(\tau)$, $j = 1, 2$, correspond to different spatial points. Let us note that because the different maxima are in the points with different values of $\bar{M}_\perp$, there is no reason for them to be equal. The phase trajectory in the plane (r_{10}, r_{01}) confirms the quasi-periodic character of oscillations (see figure 21).

The two-dimensional snapshots of the fields $h_2(X, Y, \tau)$ at different instants of time are shown in figure 22. One can see a visible change of the droplet shape between figures 22(*a*) and 22(*c*). The division of the 'main' droplet and the creation of the satellites are presented in figures 22(*d*) and 22(*e*). The 'main' droplet as well as the appeared satellites move from the right–hand side to the left–hand side, changing shape during an oscillatory process. The merging of the satellites with the 'main' droplet is shown in figure 22(*f*). The separation and the recombination of the 'main' droplet with its satellites could be the origin of oscillations. The shapes of the interfaces corresponding to figure 22(*e*) are presented in figure 23. Note that locations of the deformations on both interfaces are correlated.

4. The action of gravity on the moving droplets

Let us consider the action of the gravity force on the droplets dynamics in the presence of the spatial modulation of the transverse Marangoni number. We use as initial conditions

https://doi.org/10.1017/jfm.2025.11048 Published online by Cambridge University Press

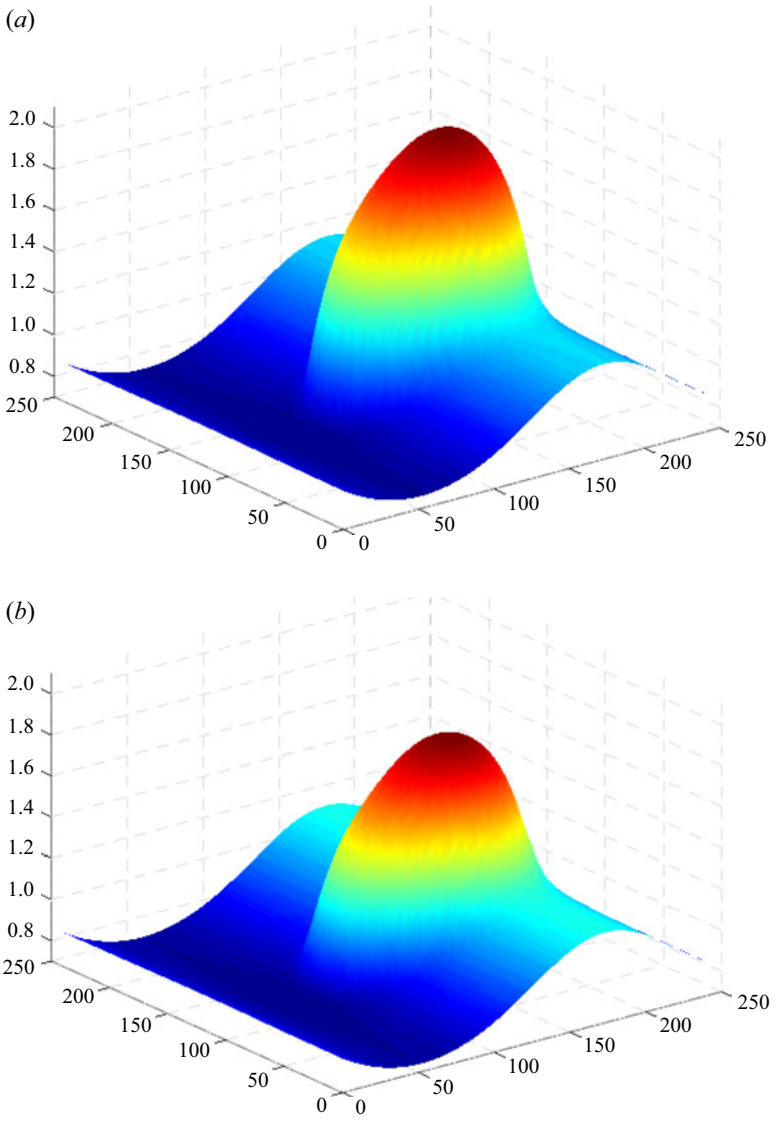


Figure 15. The shapes of interfaces (*a*) $h_2(X, Y, \tau)$ and (*b*) $h_1(X, Y, \tau)$ for $\bar{M}_\perp = -1$, $M_\parallel = 0.0001$, $\Delta_X = 0.025$, $Bo = 0.02$, $Bi = 20$, $\tau = 150\,000$.

the droplet shown in figure 12 ($Bo = 0.02$), and increase the gravity force (we take $Bo = 0.1$). The two-dimensional snapshots of the fields $h_2(X, Y, \tau)$ at different instants of time are presented in figure 24. The droplet moving from right to left is significantly flattened (cf. for instance, figures 12(*a*) and 24(*c*)). The three-dimensional shape of the interface $h_2(X, Y, \tau)$ corresponding to figure 24(*a*) is shown in figure 25.

5. The influence of the period of spatial modulation and the initial droplet radius on the droplet shape

We have also analysed the influence of the period of spatial modulation L, and the initial droplet radius R, on the shape and the motion of the droplet.

https://doi.org/10.1017/jfm.2025.11048 Published online by Cambridge University Press

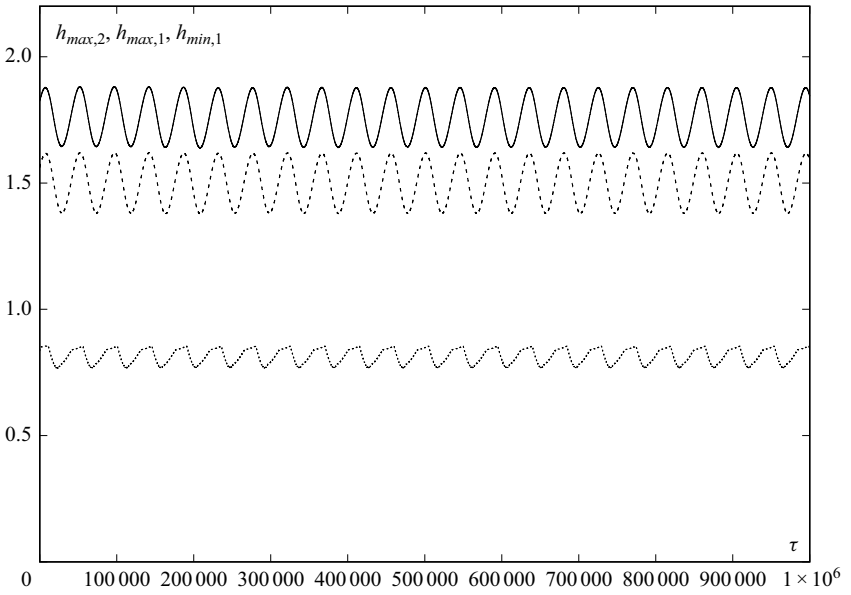


Figure 16. The temporal evolution of $h_{max,2}(\tau)$ (solid line), $h_{max,1}(\tau)$ (dashed line) and $h_{min,1}(\tau)$ (dotted line) for $\bar{M}_\perp = -1$, $M_\parallel = 0.001$, $\Delta_X = 0.025$, $Bo = 0.02$, $Bi = 20$.

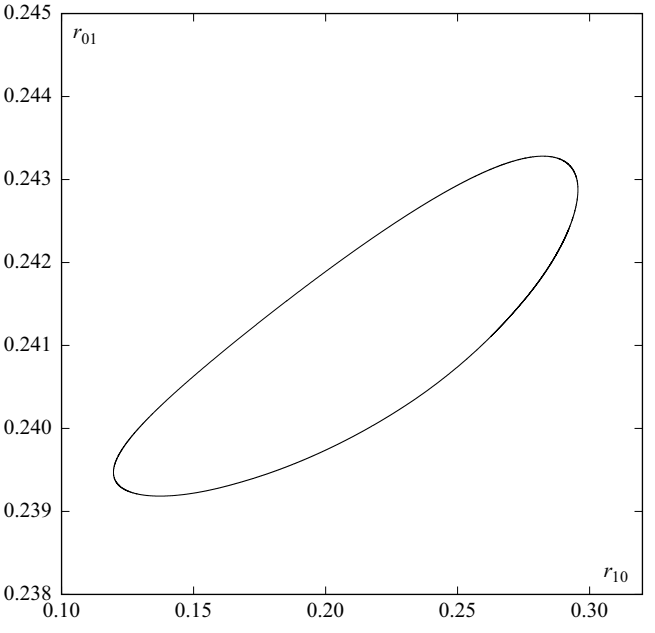


Figure 17. The phase trajectory in the plane (r_{10}, r_{01}) for $\bar{M}_\perp = -1$, $M_\parallel = 0.001$, $\Delta_X = 0.025$, $Bo = 0.02$, $Bi = 20$.

https://doi.org/10.1017/jfm.2025.11048 Published online by Cambridge University Press

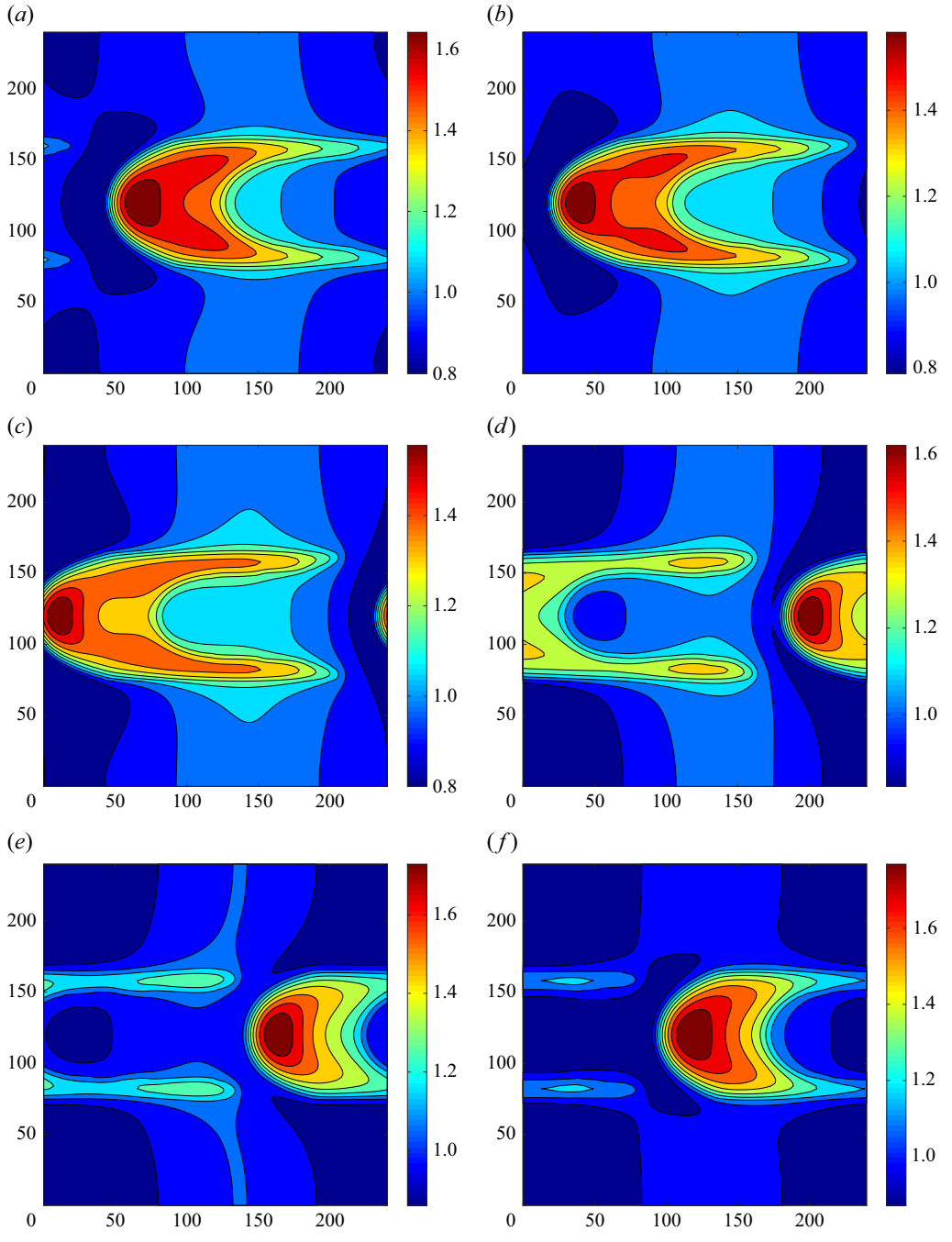


Figure 18. The fields of $h_2(X, Y, \tau)$ for $\bar{M}_\perp = -1$, $M_\parallel = 0.001$, $\Delta_X = 0.025$, $Bo = 0.02$, $Bi = 20$, for (*a*) $\tau = 300\,000$, (*b*) $\tau = 308\,500$, (*c*) $\tau = 315\,000$, (*d*) $\tau = 323\,500$, (*e*) $\tau = 331\,200$, (*f*) 336 000.

https://doi.org/10.1017/jfm.2025.11048 Published online by Cambridge University Press

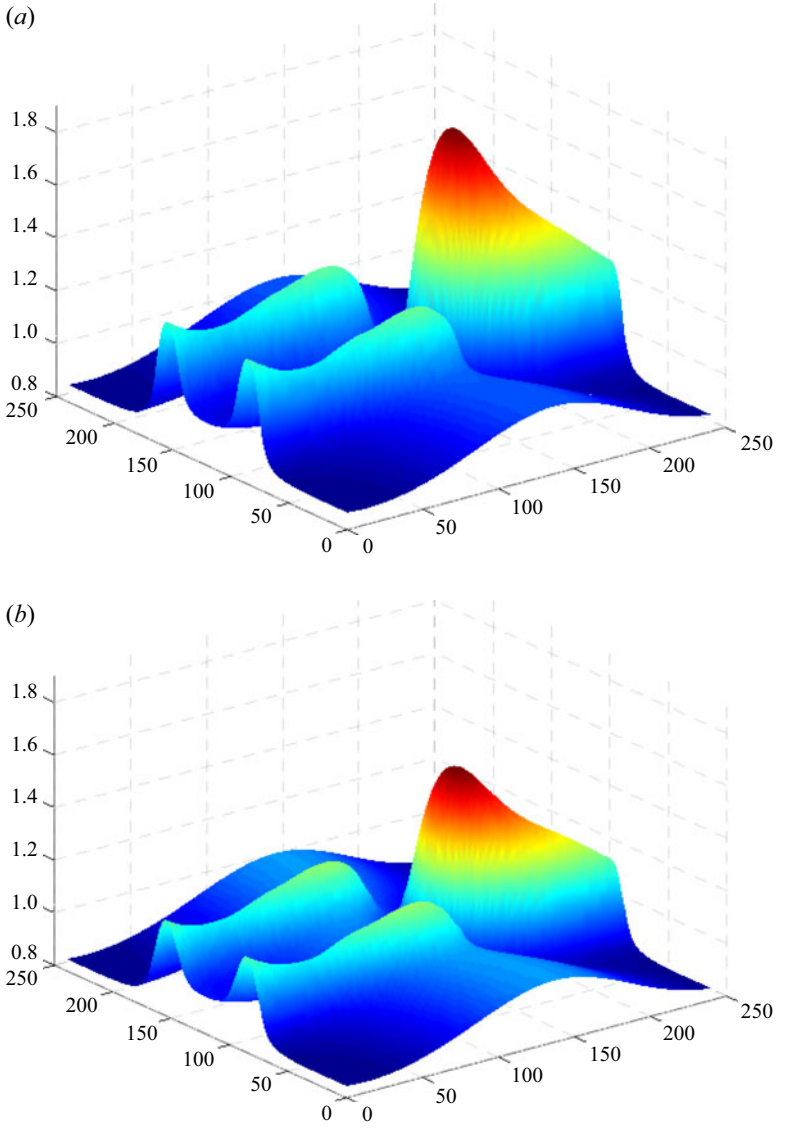


Figure 19. The shapes of interfaces (*a*) $h_2(X, Y, \tau)$ and (*b*) $h_1(X, Y, \tau)$ for $\bar{M}_\perp = -1$, $M_\parallel = 0.001$, $\Delta_X = 0.025$, $Bo = 0.02$, $Bi = 20$, $\tau = 331\,200$.

The influence of the enhancement of L is twofold. First, according to (3.8), the spatial gradient of $M_\perp(X)$ is diminished. Second, the distance between the droplets that form a periodic sequence is enhanced, hence the interaction between them is weakened. We made simulations in the computational region $2L \times 2L$, taking the grid 240×240. We got periodic oscillations of a single droplet again. The two-dimensional snapshots of the fields $h_2(X, Y, \tau)$ at different instants of time are shown in figure 26. One can see the creation of satellites in figures 26(*c*) and 26(*d*). The 'main' droplet as well as the appeared satellites move from right to left, changing shape during an oscillatory process.

Comparison of figures 18 and 26 shows that the swallow-tail shape of the droplet persists. The enhancement of the droplet size (see figure 27) restores the interaction of the droplets but does not qualitatively change their shape.

https://doi.org/10.1017/jfm.2025.11048 Published online by Cambridge University Press

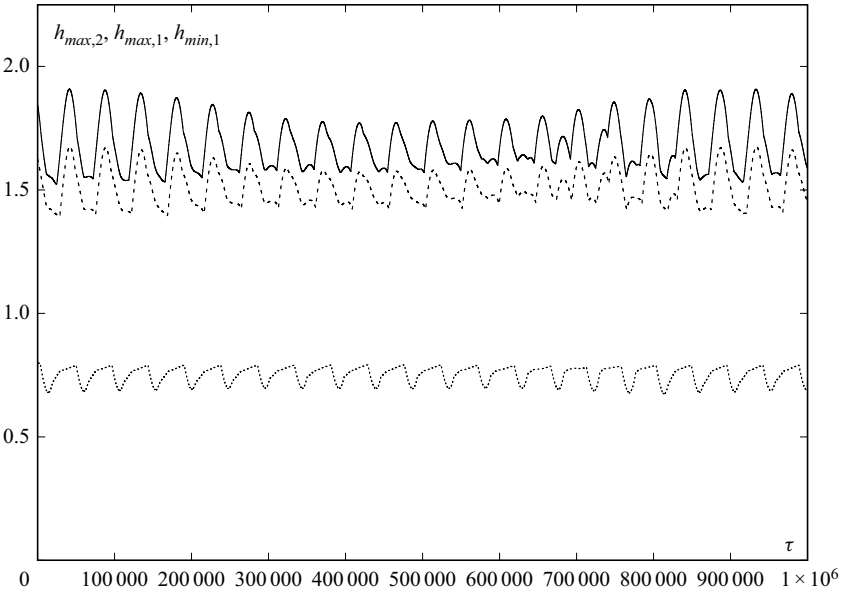


Figure 20. The temporal evolution of $h_{max,2}(\tau)$ (solid line), $h_{max,1}(\tau)$ (dashed line) and $h_{min,1}(\tau)$ (dotted line) for $\bar{M}_\perp = -1$, $M_\parallel = 0.001$, $\Delta_X = 0.05$, $Bo = 0.02$, $Bi = 20$.

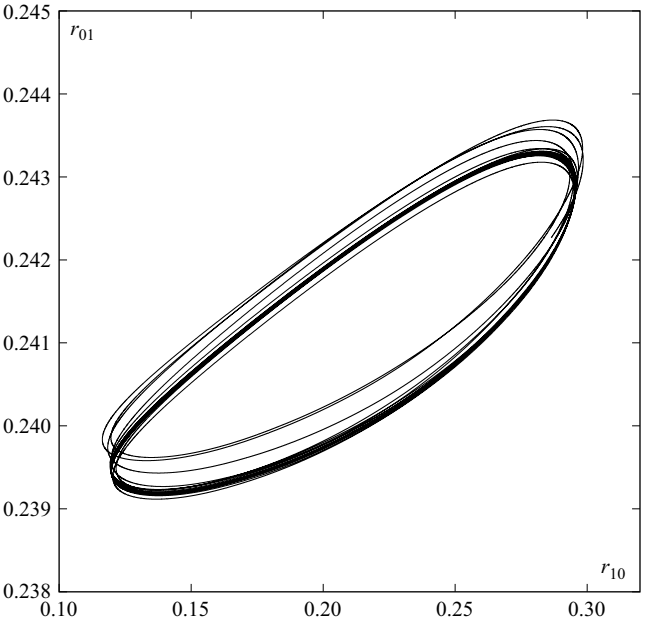


Figure 21. The phase trajectory in the plane (r_{10}, r_{01}) for $\bar{M}_\perp = -1$, $M_\parallel = 0.001$, $\Delta_X = 0.05$, $Bo = 0.02$, $Bi = 20$.

https://doi.org/10.1017/jfm.2025.11048 Published online by Cambridge University Press

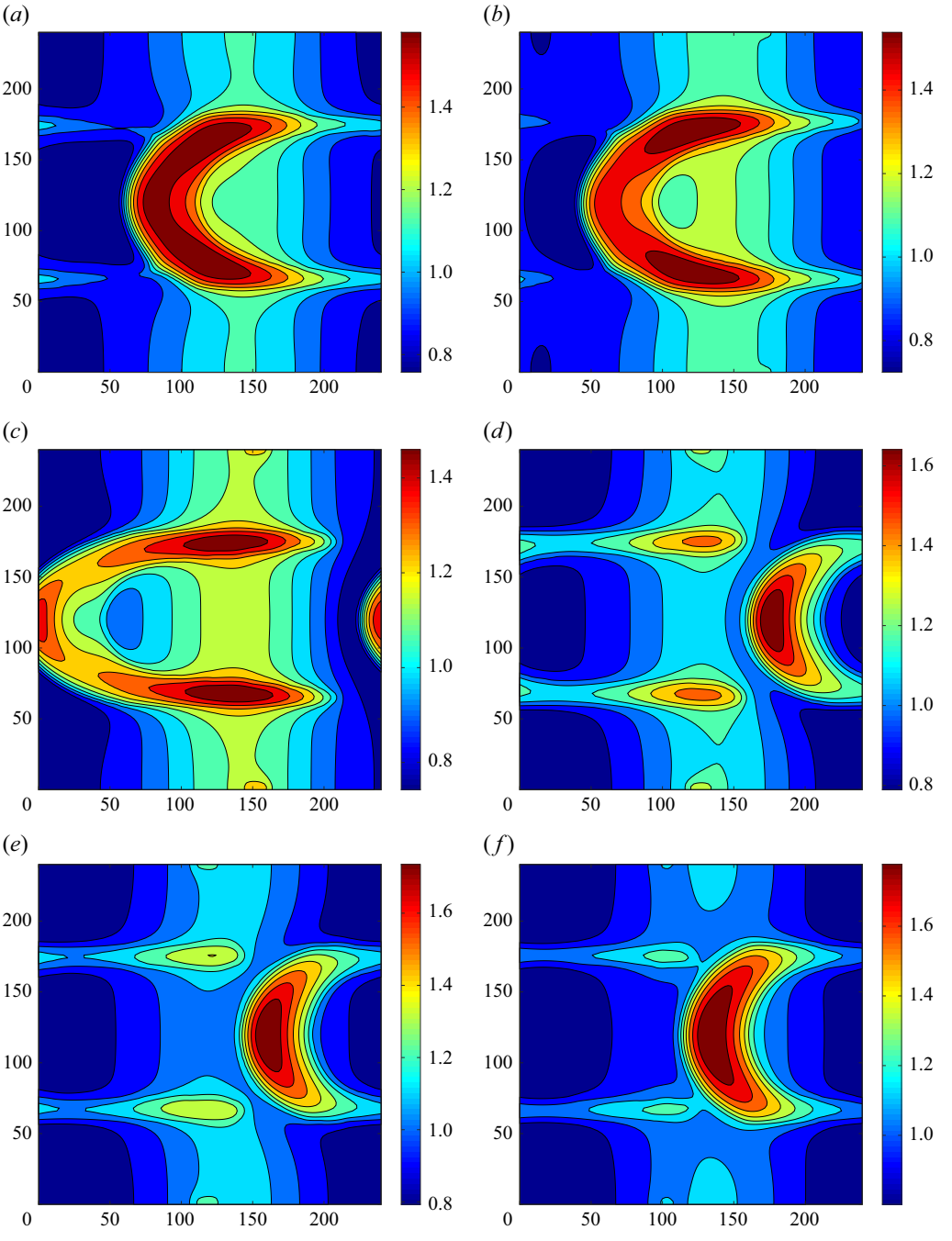


Figure 22. The fields of $h_2(X, Y, \tau)$ for $\bar{M}_\perp = -1$, $M_\parallel = 0.001$, $\Delta_X = 0.05$, $Bo = 0.02$, $Bi = 20$, for (*a*) $\tau = 100\,000$, (*b*) $\tau = 104\,000$, (*c*) $\tau = 112\,500$, (*d*) $\tau = 125\,000$, (*e*) $\tau = 129\,000$, (*f*) $\tau = 135\,700$.

https://doi.org/10.1017/jfm.2025.11048 Published online by Cambridge University Press

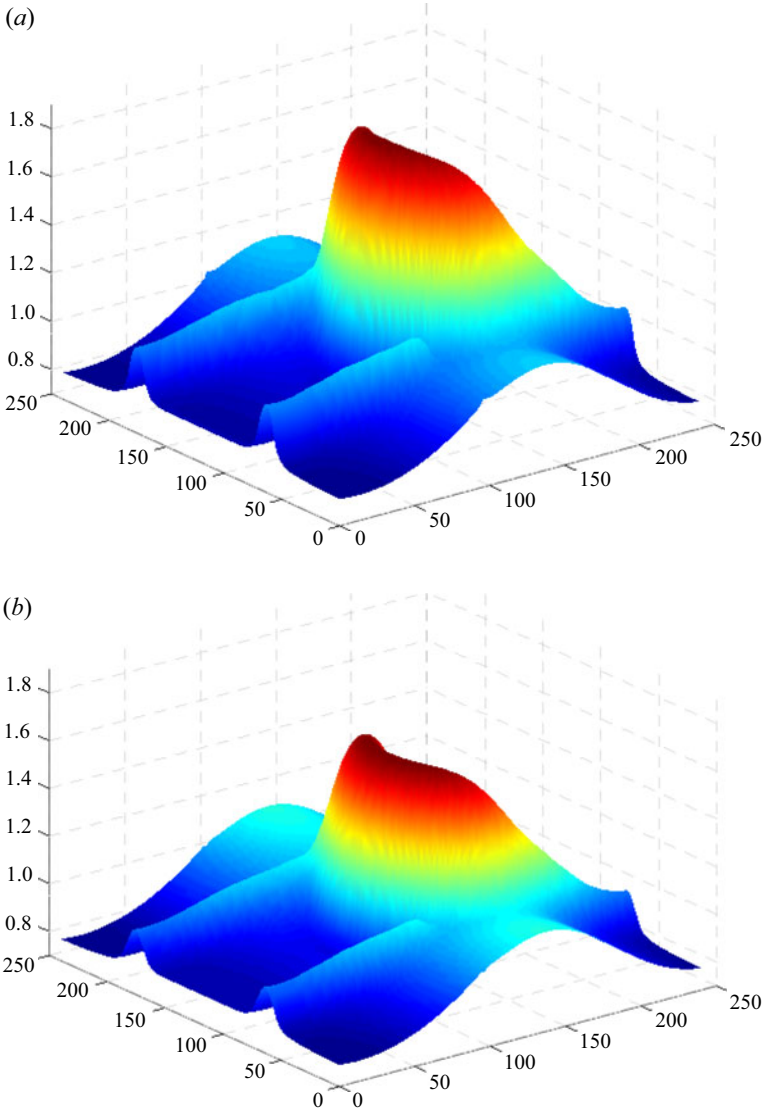


Figure 23. The shapes of interfaces (*a*) $h_2(X, Y, \tau)$ and (*b*) $h_1(X, Y, \tau)$ for $\bar{M}_\perp = -1$, $M_\parallel = 0.001$, $\Delta_X = 0.05$, $Bo = 0.02$, $Bi = 20$, $\tau = 129\,000$.

6. Conclusions

We have analysed the development of the longwave deformational instability of a floating droplet under the action of an inclined temperature gradient in the presence of the spatial modulation of the transverse temperature gradient. The problem has been studied numerically in the framework of the longwave approximation and the precursor model. The evolution equations were discretised by central differences for spatial derivatives, and solved using an explicit scheme. Periodic boundary conditions have been applied on the boundaries of the computational region.

It is shown that the spatial modulation of the transverse Marangoni number is accompanied by the change of the droplet shape and can lead to development of periodic

https://doi.org/10.1017/jfm.2025.11048 Published online by Cambridge University Press

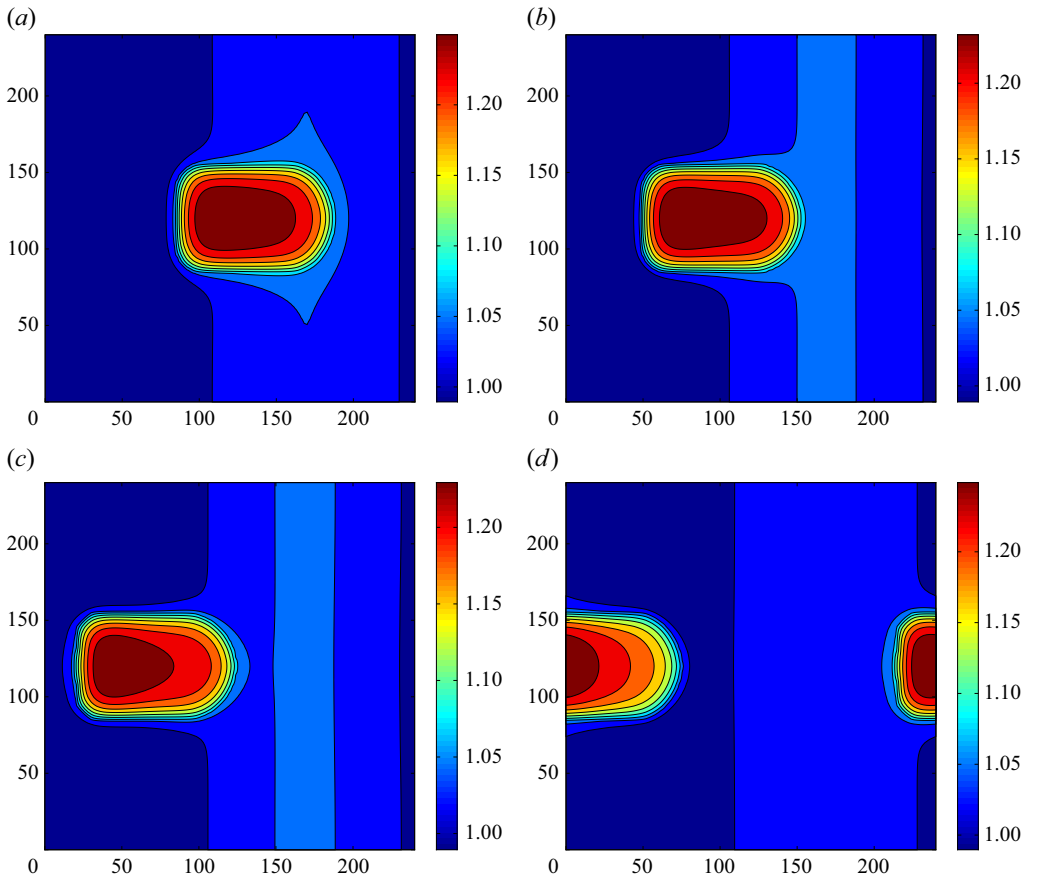


Figure 24. The fields of $h_2(X, Y, \tau)$ for $\bar{M}_\perp = -1$, $M_\parallel = 0.0001$, $\Delta_X = 0.025$, $Bo = 0.1$, $Bi = 20$, for (*a*) $\tau = 100\,000$, (*b*) $\tau = 180\,000$, (*c*) $\tau = 260\,000$, (*d*) $\tau = 340\,000$.

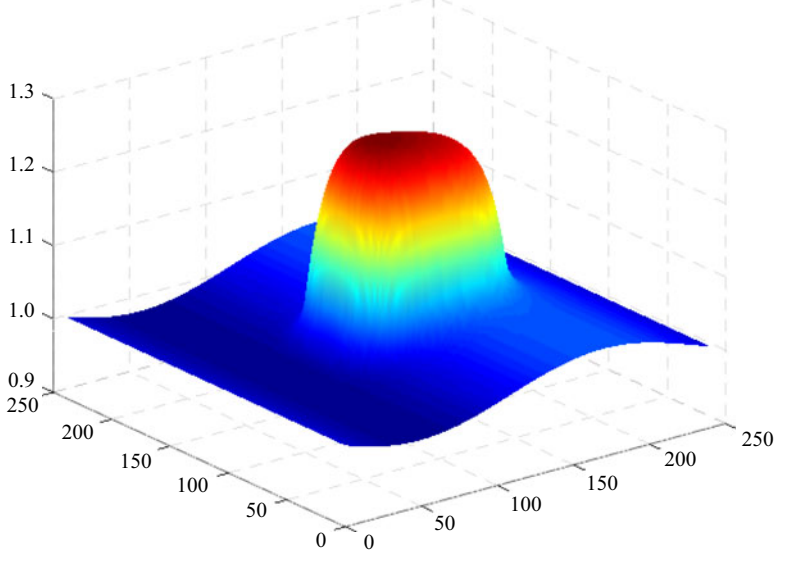


Figure 25. The shape of the interface $h_2(X, Y, \tau)$ for $\bar{M}_\perp = -1$, $M_\parallel = 0.0001$, $\Delta_X = 0.025$, $Bo = 0.1$, $Bi = 20$, $\tau = 100\,000$.

https://doi.org/10.1017/jfm.2025.11048 Published online by Cambridge University Press

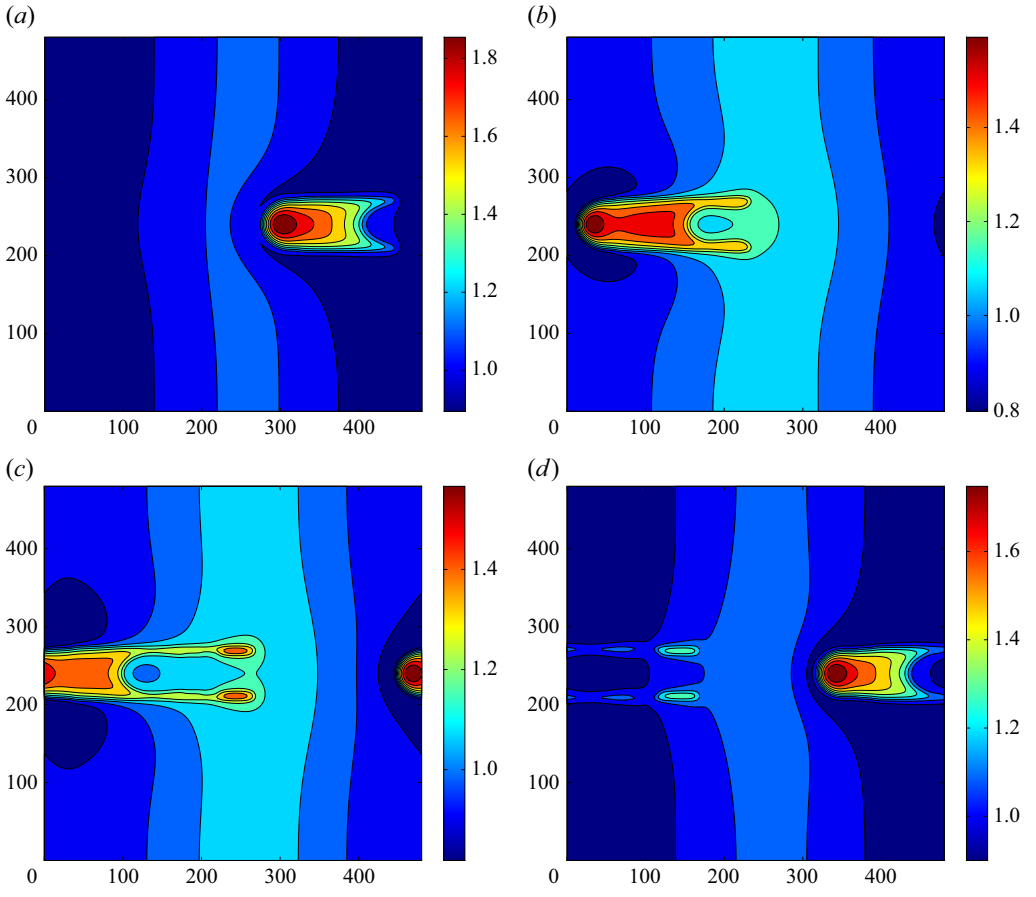


Figure 26. The fields of $h_2(X, Y, \tau)$ for $\bar{M}_\perp = -1$, $M_\parallel = 0.001$, $\Delta_X = 0.025$, $R = 20$, $Bo = 0.02$, $Bi = 20$, for (*a*) $\tau = 530\,000$, (*b*) $\tau = 552\,500$, (*c*) $\tau = 560\,000$, (*d*) $\tau = 578\,500$, with $L = 480$ and grid 240×240.

oscillations. The period of oscillations coincides with the time of passing by the droplet the distance L, equal to the spatial period of the temperature modulation. At the definite region of parameters, the quasi-periodic oscillations accompanied by the creation of the pulsating satellites have been obtained. The separation and the recombination of the 'main' droplet with the satellites can be the origin of oscillations.

The flow regimes described in the paper can be observed under microgravity conditions. Specifically, the values of parameters $M_\perp$ and Bo can be reached in an experiment under normal gravity $g = g_0 = 9.8$ m s^{-2} in the case $H_1^0 \sim 5$ μm, or under reduced gravity $g = 10^{-5} g_0$ for $H_1^0 \sim 1.5$ mm. We choose the following values of parameters: $\eta_1 = 2.55 \times 10^{-2}$ kg m^{-1} s^{-1}, $\rho_1 = 1.94 \times 10^3$ kg m^{-3} and $\sigma_1^0 = 7.6 \times 10^{-3}$ N m^{-1}. Taking $L^* = 5 \times 10^{-5}$ m and $U = 0.01$ m s^{-1}, we get that the Reynolds number is rather small ($Re = U * \rho_1 * L^*/\eta_1 = 0.038$). The smallness of Re validates using the lubrication approximation. The estimates presented above show the feasibility of possible experimental demonstration of effects considered in the paper. The value $M_\perp = -1$ used in our computations corresponds to the temperature difference $T_s - T_g = 1$ K, which can be reached in an experiment.

Declaration of interests. The authors report no conflict of interest.

https://doi.org/10.1017/jfm.2025.11048 Published online by Cambridge University Press

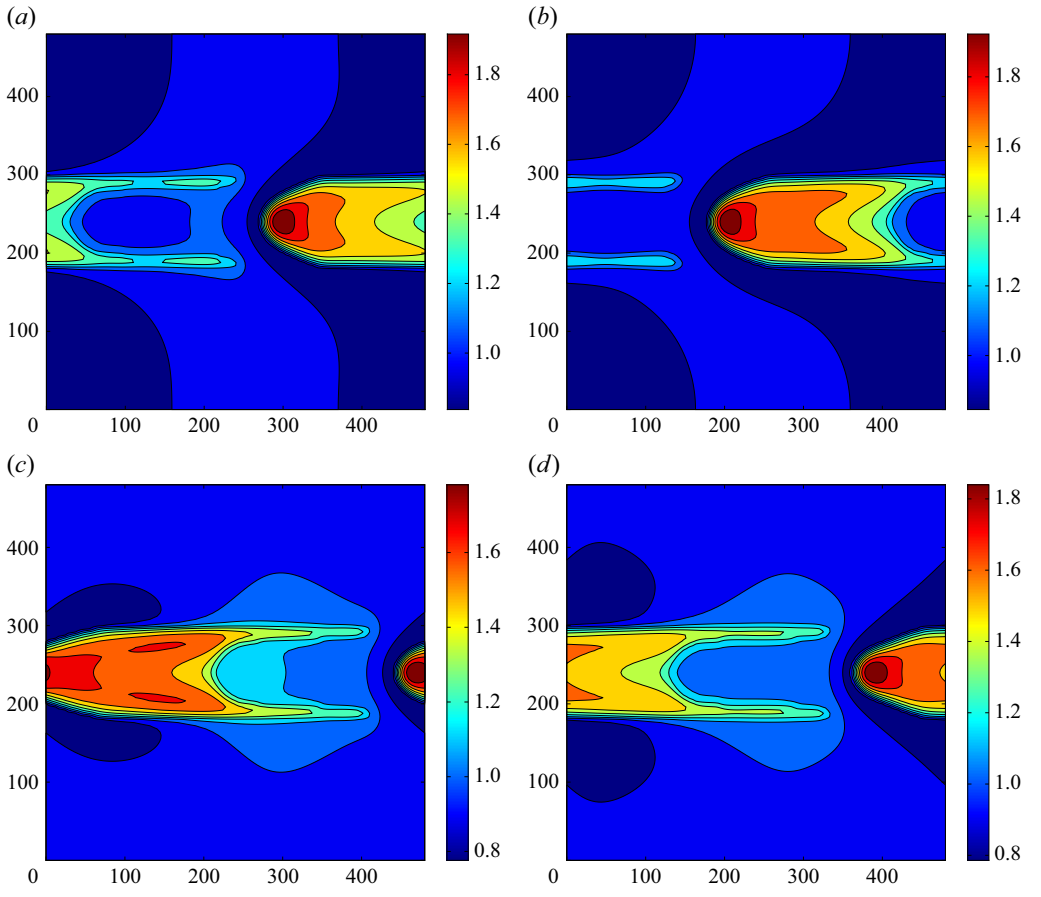


Figure 27. The fields of $h_2(X, Y, \tau)$ for $\bar{M}_\perp = -1$, $M_\parallel = 0.001$, $\Delta_\chi = 0.025$, $R = 40$, $Bo = 0.02$, $Bi = 20$, for (*a*) $\tau = 410\,000$, (*b*) $\tau = 418\,500$, (*c*) $\tau = 430\,000$, (*d*) $\tau = 438\,500$, with $L = 480$ and grid 240×240.

Appendix. Validation of the results

In this appendix, we present more details on the numerical scheme and the validation of the results. Recall that we assume that the characteristic horizontal scale of the surface deformations is significantly larger than the thickness of the droplet and that of the substrate layer typically chosen as the length scale. The distance between the grid nodes can be chosen rather large.

The simulations have been carried out during at least 10^6 non-dimensional time units. In all the simulations, the change of the fields h_j, $j = 1, 2$, was less than 0.1 %. The time step typically was changed between 0.00125 and 0.005, which is significantly below the linear scheme stability boundary. No quantitative changes have been observed for simulations made with different time steps.

For the steady state presented in figure 4, the maximum values of variables h_2 were equal to 1.6801 (grid 100×100), 1.6803 (120×120) and 1.6803 (160×160). For the periodic oscillations presented in figure 16, the maximum values of variables h_2 were equal to 1.8497 (grid 100×100), 1.8505 (120×120) and 1.8506 (160×160). We also made the following test: we have compared the fields obtained from the Gaussian initial distribution

https://doi.org/10.1017/jfm.2025.11048 Published online by Cambridge University Press

with the fields obtained from the previous state (after $\tau = 1 \times 10^6$ non-dimensional units). The fields h_j, $j = 1, 2$, were indistinguishable.

References

Bacri, L., Debrégeas, G. & Brochard-Wyart, F. 1996 Experimental study of the spreading of a viscous droplet on a nonviscous liquid. *Langmuir* **12**, 6708.

Brochard Wyart, F., Martin, P. & Redon, C. 1993 Liquid/liquid dewetting. *Langmuir* **9**, 3682.

Buffone, C. 2019 Formation, stability and hydrothermal waves in evaporating liquid lenses. *Soft Matter* **15**, 1970.

Davis, S.H. 1987 Thermocapillary instabilities. *Annu. Rev. Fluid Mech.* **19**, 403.

Géoris, P., Hennenberg, M., Lebon, G. & Legros, J.C. 1999 Investigation of thermocapillary convection in a three-liquid-layer system. *J. Fluid Mech.* **389**, 209.

Greco, E.F. & Grigoriev, R.O. 2009 Thermocapillary migration of interfacial droplets. *Phys. Fluids* **21**, 042105.

Joanny, J.F. 1987 Wetting of a liquid substrate. *Physico-Chem. Hydrodyn.* **9**, 183.

Ju, G., Yang, X., Li, L., Cheng, M. & Shi, F. 2019 Removal of oil spills through a self-propelled smart device. *Chem. Asian J.* **14**, 2435.

Labanieh, L., Nguyen, T.N., Zhao, W.A. & Kang, D.K. 2015 Floating droplet array: an ultrahigh-throughput device for droplet trapping, real time analysis and recovery. *Micromachines* **60**, 1469.

Nepomnyashchy, A. 2021 Droplet on a liquid substrate: wetting, dewetting, dynamics, instabilities. *Curr. Opin. Colloid Interface Sci.* **51**, 101398.

Nepomnyashchy, A.A. & Simanovskii, I.B. 2007 Marangoni instability in ultrathin two-layer films. *Phys. Fluids* **19**, 122103.

Nepomnyashchy, A.A. & Simanovskii, I.B. 2009*a* Dynamics of ultra-thin two-layer films under the action of inclined temperature gradients. *J. Fluid Mech.* **631**, 165.

Nepomnyashchy, A.A. & Simanovskii, I.B. 2009*b* Instabilities and ordered patterns in nonisothermal ultrathin bilayer fluid films. *Phys. Rev. Lett.* **102**, 164501.

Nepomnyashchy, A. & Simanovskii, I. 2012 Nonlinear Marangoni waves in a two-layer film in the presence of gravity. *Phys. Fluids* **24**, 032101.

Nepomnyashchy, A.A. & Simanovskii, I.B. 2021 Droplets on the liquid substrate: thermocapillary oscillatory instability. *Phys. Rev. Fluids* **6**, 034001.

Nepomnyashchy, A.A. & Simanovskii, I.B. 2025 Dynamics of floating droplets under the action of an inclined temperature gradient. *J. Fluid Mech.* **1007**, A51.

Nepomnyashchy, A.A., Simanovskii, I.B. & Braverman, L.M. 2001 Stability of thermocapillary flows with inclined temperature gradient. *J. Fluid Mech.* **442**, 141.

Nepomnyashchy, A.A., Simanovskii, I.B. & Legros, J.C. 2012 *Interfacial Convection in Multilayer Systems*, 2nd edn. Springer.

Oron, A., Davis, S.H. & Bankoff, S.G. 1997 Long-scale evolution of thin liquid films. *Rev. Mod. Phys.* **69**, 931.

Pearson, J.R. 1958 On convection cells induced by surface tension. *J. Fluid Mech.* **4**, 489.

Pototsky, A., Bestehorn, M., Merkt, D. & Thiele, U. 2005 Morphology changes in the evolution of liquid two-layer films. *J. Chem. Phys.* **122**, 224711.

Rybalko, S., Magome, N. & Yoshikawa, K. 2004 Forward and backward laser-guided motion of an oil droplet. *Phys. Rev. E* **70**, 046301.

Scriven, L.E. & Sternling, C.V. 1964 On cellular convection driven by surface-tension gradients: effects of mean surface tension and surface viscosity. *J. Fluid Mech.* **19**, 321.

Simanovskii, I.B. & Nepomnyashchy, A.A. 1993 *Convective Instabilities in Systems with Interface*. Gordon and Breach.

Song, C., Moon, J.K., Lee, K., Kim, K. & Pak, H.K. 2014 Breathing, crawling, budding, and splitting of a liquid droplet under laser heating. *Soft Matter* **10**, 2679.

Suciu, D.G., Smigelschi, O. & Ruckenstein, E. 1970 The spreading of liquids on liquids. *J. Colloid Interface Sci.* **33**, 520.

Ueno, I., Kurosawa, T. & Kawamura, H. 2002 Thermocapillary convection in thin liquid layer with temperature gradient inclined to free surface. In *Heat Transfer 2002, Proceedings of the 12th International Heat Transfer Conference (Grenoble, France, August 18-23)*, p. 129.

Van Hook, S.J., Schatz, M.F., McCormick, W.D., Swift, J.B. & Swinney, H.L. 1995 Long-wavelength instability in surface-tension-driven Bénard convection. *Phys. Rev. Lett.* **75**, 4397.

https://doi.org/10.1017/jfm.2025.11048 Published online by Cambridge University Press

VAN HOOK, S.J., SCHATZ, M.F., SWIFT, J.B., MCCORMICK, W.D. & SWINNEY, H.L. 1997 Long-wavelength surface-tension-driven Bénard convection: experiment and theory. *J. Fluid Mech.* **345**, 45.

YAKSHI-TAFTI, E., CHO, HJ. & KUMAR, R. 2010 Droplet actuation on a liquid layer due to thermocapillary motion: shape effect. *Appl. Phys. Lett.* **96**, 264101.

YAMINI, Y., REZAZADEH, M. & SEIDI, S. 2019 Liquid-phase microextraction – the different principles and configurations. *TrAC Trends Anal. Chem.* **112**, 264.

ZHENG, Z. & STONE, H. 2021 The influence of boundaries on gravity currents and thin films: drainage, confinement, convergence and deformation effects. *Annu. Rev. Fluid Mech.* **54**, 27.

https://doi.org/10.1017/jfm.2025.11048 Published online by Cambridge University Press